

Imaging and addressing of neutral atoms inside a fiber cavity

José Eduardo Uruñuela Castellero

Masterarbeit in Physik
angefertigt im Institut für Angewandte Physik

vorgelegt der
Mathematisch-Naturwissenschaftlichen Fakultät
der
Rheinischen Friedrich-Wilhelms-Universität
Bonn

JUNE 2017

I hereby declare that this thesis was formulated by myself and that no sources or tools other than those cited were used.

Bonn,
Date

.....
Signature

1. Gutachter: Prof. Dieter Meschede
2. Gutachter: Prof. Stefan Linden

Contents

1	Introduction	1
2	Fluorescence imaging of atoms inside the cavity	5
2.1	Overview of the imaging technique with the D1 line	7
2.1.1	Illumination scheme	7
2.1.2	Basic theory of fluorescence imaging	8
2.2	Experimental setup for imaging using the D1 line	10
2.2.1	Light sources for the illumination beams	10
2.2.2	Stabilization of the laser frequencies with polarization spectroscopy	12
2.2.3	Frequency shifting setup	15
2.2.4	Optimization of the optical imaging system	16
2.3	Results and characterization of the new imaging scheme	18
2.3.1	Calibration of the magnification factor	18
2.3.2	Optimization of the illumination frequency and power	20
2.4	Conclusions and next steps	21
3	Optical addressing of atoms in an optical lattice	23
3.1	Implementation of the addressing system	24
3.1.1	The push-out technique	24
3.1.2	Beam steering with an acousto-optic deflector	25
3.1.3	Optical transfer system	28
3.2	Characterization and optimization of the addressing system	29
3.2.1	Dependence of the push-out effect on the beam power	30
3.2.2	Calibration of the push-out beam displacement	32
3.3	Conclusions and next steps	32
4	Summary and outlook	35
A	Effective scattering rate in a three-level system with two light fields	45

Introduction

Since Einstein's groundbreaking explanation of the absorption and emission of electromagnetic radiation by atoms in 1917 [1, 2], matter-light interaction at the quantum level has been subject of extensive research. During the years that followed, most of the observed effects of this interaction could be well described by the semi-classical theory, see e.g. [3]. Nevertheless, the fundamental phenomenon of spontaneous decay of an excited atom by the emission of a photon, could not be accurately explained until Dirac formulated the quantization of the electromagnetic field in 1927 [4]. With the theory of Quantum Electrodynamics (QED), spontaneous emission was understood as resulting from the coupling of an atom with the *zero-point* energy fluctuations of the radiation field in the surrounding medium.

Later, in 1946, Purcell discovered that the rate of spontaneous emission of an atom could be modified by imposing boundary conditions [5], such as two parallel mirrors forming a cavity, hence restricting the available modes of the electromagnetic field. This seminal paper gave birth to the field of Cavity Quantum Electrodynamics (CQED). A comprehensive discussion of this field from an experimental point of view is found in the book by Haroche and Raimond [6]. The most fundamental system of this kind, a single two-level atom interacting with a single electromagnetic mode of the cavity, can be described by the Jaynes-Cummings model [7]. The electric-dipole coupling rate g , which describes the strength of the interaction between the atom and the field, depends on the mode volume of the cavity: $g \propto V^{-1/2}$. A more realistic scenario (shown in Figure 1.1a) takes into account the decay processes of the system due to its interaction with the environment: the atom can spontaneously emit a photon in free space with a scattering rate γ , and the photons can leak out of the resonator at a rate 2κ with the cavity field damping rate κ . A standard figure of merit of the atom-photon interaction in these systems is the *cooperativity*, defined as $C = \frac{g^2}{2\kappa\gamma}$. Particularly interesting effects arise if a photon emitted by the atom has a high probability of being reabsorbed by the same atom before escaping the cavity, e.g. $g \gg \kappa, \gamma$. This is the so called strong-coupling regime, where the atom couples coherently to the *vacuum state* of the cavity mode [8].

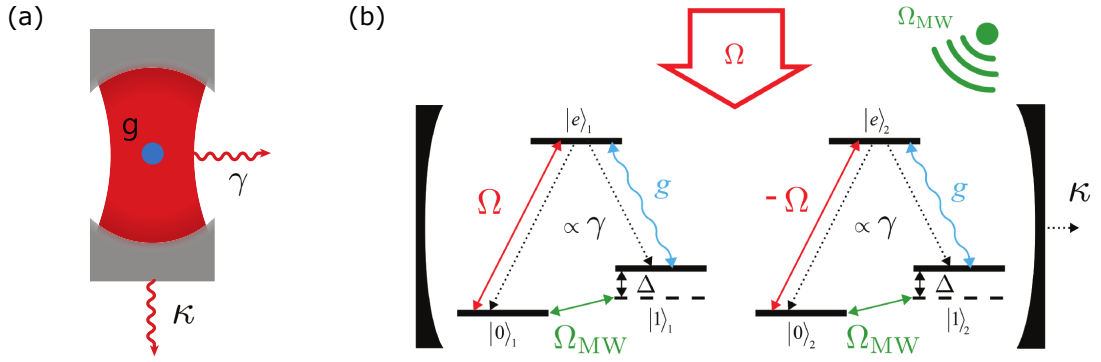


Figure 1.1: **Dissipative preparation of entanglement with an optical cavity.** (a) Fundamental Cavity-QED system: a single two-level atom interacts with a single mode of the cavity with dipole-coupling strength g . The relaxation channels of the system are the leakage of photons at the cavity decay rate κ and the spontaneous decay of the atom by emitting photons out of the cavity mode at rate γ . (b) Schematic of the dissipative bipartite entanglement protocol inside an optical cavity proposed by [9, 10] (adapted). The identical two three-level atoms are globally addressed by a resonant driving field, the intra-cavity field and a detuned microwave field (or Raman beam), with respective strengths Ω , g and Ω_{MW} . Spontaneous emission γ and cavity photon loss κ serve as dissipation channels.

In more recent times, experimental atom-cavity systems have gained much interest as powerful tools for Quantum Information [11, 12]. A review of experimental techniques used in such CQED systems can be found in [13]. For instance it has been shown that they can be used to store the quantum information of single photons and retrieve it later, showing their potential to work as repeaters in a quantum network [14, 15]. On another side, these systems can also open the door to study more fundamental quantum effects, such as entanglement [16]. In fact, they could allow the creation of fully entangled steady states of multiple particles through dissipation, by properly engineering the decay channels, as shown recently in novel theoretical proposals [9, 10, 17, 18, 19]. The main advantages of such dissipative entanglement preparation schemes, are their independence from the initial state of the system, the robustness of the target state against disturbances, and the use of pure non-local addressing.

In this regard, presently, one major aim of our research group is to realize the first experimental implementation of dissipative bipartite entanglement, following the protocol proposed by [9, 10]. To implement the protocol, two three-level atoms need to be positioned inside the optical Fabry-Perot cavity such that they couple identically to the resonant cavity mode. It has been shown that, through dissipative state engineering, the system can be unidirectionally pumped to the maximally entangled singlet state

$$|S\rangle = \frac{1}{\sqrt{2}} (|0\rangle_1 |1\rangle_2 - |1\rangle_1 |0\rangle_2) = \frac{1}{\sqrt{2}} (|01\rangle - |10\rangle) ,$$

where $|0\rangle_i$ and $|1\rangle_i$ are two hyperfine ground states of atom i . As shown in Figure 1.1b, both atoms are globally addressed with different fields. A resonant beam coherently drives the transition between $|0\rangle$ and the excited state $|e\rangle$, while the atom-cavity interaction connects $|e\rangle$ and $|1\rangle$. Finally, a detuned microwave field or Raman beam couples the two ground states. A fundamental requirement of the protocol is a phase difference of the laser driving field of $e^{-i\pi} = -1$ between the two atoms. This condition is fulfilled if the two atoms are trapped in optical lattice potentials with a relative distance along the driving beam axis of $\Delta y = (2n + 1)\lambda/2$ for $n \in \mathbb{N}$.

For the physical implementation this translates into two main demands. First, we require an optical cavity coupled to atoms in the strong coupling regime, i.e. with $C > 1$, and the already mentioned addressing fields. Second, we need precise control of the atom number and their relative position inside the cavity mode. The first condition is already fulfilled by our main experimental setup, while to satisfy the second condition additional systems were needed, and their implementation is the central topic of this thesis.

In the following I give an overview of our experimental apparatus, shown in a simplified scheme in Figure 1.2. For a more detailed description refer to [20]. We use a fiber-based optical Fabry-Pérot cavity [21], produced in our group [22] and placed inside an ultra-high vacuum (UHV) system, coupled with the D2 line of neutral ^{87}Rb atoms (780 nm). Due to the small mode volume of the resonator ($w_0 \approx 5 \mu\text{m}$), it provides a high coupling strength ($g/2\pi \approx 80 \text{ MHz}$) with relatively fast leakage rate that characterizes an *open cavity* ($\kappa/2\pi \approx 120 \text{ MHz}$). The latter is advantageous to act on the system or retrieve information from it with high efficiency. The cooperativity is $C \approx 9$ with $\gamma_{\text{Rb,D2}}/2\pi \approx 3 \text{ MHz}$. The cavity length is stabilized using a 770 nm *lock* laser tuned such that the cavity is on resonance with both the lock laser and the ^{87}Rb D2 line. A magneto-optical trap (MOT) of ^{87}Rb atoms is created at 1 mm away from the cavity due to the limited optical access. Cold atoms from the MOT are loaded into an optical lattice ($\lambda = 860 \text{ nm}$, far detuned from atomic resonances), and then transported to the center of the cavity via an *optical conveyor belt* [23] along the horizontal axis y . There, the atoms are confined in the three directions by the use of an additional red-detuned optical lattice (on the horizontal xy -plane) and the intra-cavity standing wave of the lock laser (in the cavity axis z). The trap depths of the horizontal lattice are 1.2 mK and 0.5 mK in the x and y directions respectively. Four aspheric lenses with high numerical aperture ($NA \approx 0.5$), mounted inside the vacuum, are used to tightly focus the red-detuned trap beams. For imaging the atoms with high resolution, we illuminate them with counter-propagating light along the y -axis, near-resonant with the D2 line. One of the high-NA lenses (aligned with the x -axis) collects a fraction of the emitted fluorescence, that is detected with an EMCCD camera. Additionally, a weak beam at 780 nm sent through the cavity serves to probe the atom-cavity system; its back-reflection is detected with a single-photon counter module (SPCM). We have observed that the simultaneous resonance of the cavity and the illumination beam with the atoms cause inconsistent imaging, as will be discussed further on in the text.

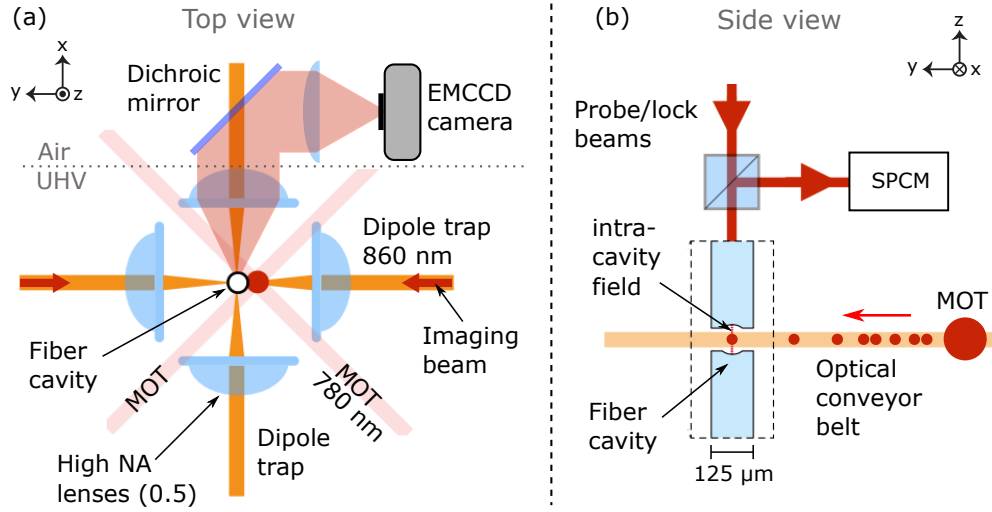


Figure 1.2: **Our fiber-cavity experimental setup** [20]. (a) View from the top showing the main components of the system used to trap ^{87}Rb atoms in a 3D optical lattice inside the cavity. We image the atoms by shining a near-resonant illumination beam along both direction of the y -axis, collecting the induced fluorescence with one of the high-NA lenses along the x -axis and detecting it with an EMCCD camera. (b) View from the side that shows how the atoms are loaded from the MOT into the dipole trap and transported to the cavity center with an optical conveyor belt. We probe the atom-cavity system by detecting the back-reflection of a weak beam with an SPCM.

In this work, I present the two experimental systems I developed and implemented to satisfy the second condition for the implementation of the dissipative entanglement protocol. That is: first to detect the position of the atoms, and then to prepare them in a given distribution. The thesis has the following structure:

In Chapter 2, an alternative technique for fluorescence imaging of the atoms inside the cavity is shown. This new technique, with illumination in the D1 line of ^{87}Rb , allows to image the atoms when they are on resonance with the cavity in a consistent and robust way, in contrast to the standard imaging with the D2 line. The high resolution images can be used to determine the position of the atoms in the lattice, with techniques already employed in other experiments of our group, but this goes beyond the reach of this work. This opens the possibility for individual addressing. In Chapter 3, I describe a setup to optically address and expel individual atoms off the optical lattice with a push-out beam. This addressing scheme will enable the selection and/or modification of particular patterns of atoms inside the cavity, thus controlling their number and relative distance. I conclude, in Chapter 4, with the discussion of the obtained results as well as with an overview of other possible future applications of the newly implemented systems.

Fluorescence imaging of atoms inside the cavity

One main condition for the implementation of the dissipative entanglement protocol is to obtain precise information about the configuration of the atomic ensemble. In particular, we need to know the number of atoms and their relative distance, in other words their positions, in the optical lattice. One common technique to retrieve this information is by fluorescence imaging: the atoms are illuminated by near-resonant light in a molasses configuration in order to cool the atoms in all directions, while some fraction of the emitted photons is collected and detected with an optical system to obtain an image. This technique has been widely used in other research groups [24, 25], and in our laboratory with high accuracy in the position determination of the atoms in the trap [26, 27, 28].

The main benefit of the usual 3D molasses configuration with red-detuned illumination, is that it offers a cooling mechanism during the imaging process, that counteracts the heating of the atoms from the photon recoil, and ensures their survival in the trap. Nevertheless, our fiber-cavity setup does not allow such configuration because the vertical axis is blocked by the cavity, and one of the available horizontal axes is reserved for the imaging system. To circumvent this issue, other groups have shown novel cavity-cooling techniques [29]. Unfortunately, the desired *open* nature of our cavity entails a large linewidth $\kappa/2\pi \approx 120$ MHz that does not allow to implement such cooling methods [20]. Inevitably, this leads to heating and the subsequent loss of atoms even for short illumination times. Therefore, presently only destructive imaging is possible in our system.

The standard method that we use for fluorescence imaging is understood by recalling the setup presented previously in Figure 1.2. An illumination laser is focused at the center of the cavity from counterpropagating direction along the y -axis, with $\text{lin}\perp\text{lin}$ polarizations. This beam is near-resonant with the D2 line of ^{87}Rb (see Fig. 2.1a) in the $\{F = 2 \rightarrow F' = 3\}$ hyperfine cycling transition. An additional weak repumper beam in the $\{F = 1 \rightarrow F' = 2\}$ transition prevents losses from off-resonant excitation that may lead to populating the $F = 1$ state. Then, part of the fluorescence emitted by the atoms

is collected by one of the high-NA lenses in the x -axis, and focused onto the chip of an EMCCD camera to form the image. In this case only 1D molasses cooling is present.

However, under this scheme we encountered a problem intrinsic to our cavity-atoms system, given that the cavity is also resonant with the D2 line for highest coupling rate with the atoms. In fact, the cavity affects the free-space scattering properties of the atoms, hindering their fluorescence detection. This effect is analyzed in detail in [20]. The issue can be clearly observed in Figure 2.1b: if the cavity is out of resonance with the D2 line, after averaging many images, we see that the fluorescence is highest in the cavity region, where the 3D optical lattice traps the atoms for a longer time. On the other hand, if both the cavity and the illumination light are resonant with the D2 light, we notice that the detected fluorescence in the cavity region diminishes significantly. This effect is mainly understood as following: due to the Purcell effect, the scattering rate of the atoms is enhanced in general; with the absence of a cooling mechanism during the imaging process, the enhanced scattering translates directly into higher heating rates and lead to a very rapid loss of the atoms from the trap; but the emission occurs mostly in the cavity mode, resulting in an overall lower fluorescence in free space.

But even in the case of a working cooling mechanism, the biggest problem is that the scattering of the atoms becomes dependent on additional factors, for instance on the coupling of individual atoms with the cavity and on the probe-cavity detuning. This is highly undesirable since it makes the fluorescence detection inconsistent and non-reproducible.

One possible solution is to move the cavity away from resonance during the imaging process. However, due to the broad linewidth of our cavity, we measured that a detuning of at least 1 GHz was needed to eliminate the effect. This is experimentally possible but technically elaborated. For this reason we chose another approach: to use the D1 line of ^{87}Rb for imaging while still keeping the cavity on resonance with the D2 line. In this way, the imaging light at 795 nm would be far from any cavity resonance, and hence insensitive to the cavity effects mentioned previously. This imaging method is still destructive but can be further combined with cooling schemes that use the D2 line, and the cooling light filtered out before detection. Yet, it was not known if imaging with the D1 line would work, since it has no cycling transition and multiple dark states are present.

In this chapter I will show that D1 fluorescence imaging is possible in our system. The first part (Sec. 2.1) gives an overview of the working principle of the new imaging technique, as well as some basic theoretical background of the physical processes involved. Subsequently in Section 2.2, I will cover the experimental steps followed for the implementation and give some relevant technical details. Finally, the last part (Sec. 2.3) describes the optimization process of the imaging parameters and reports the first results of the project.

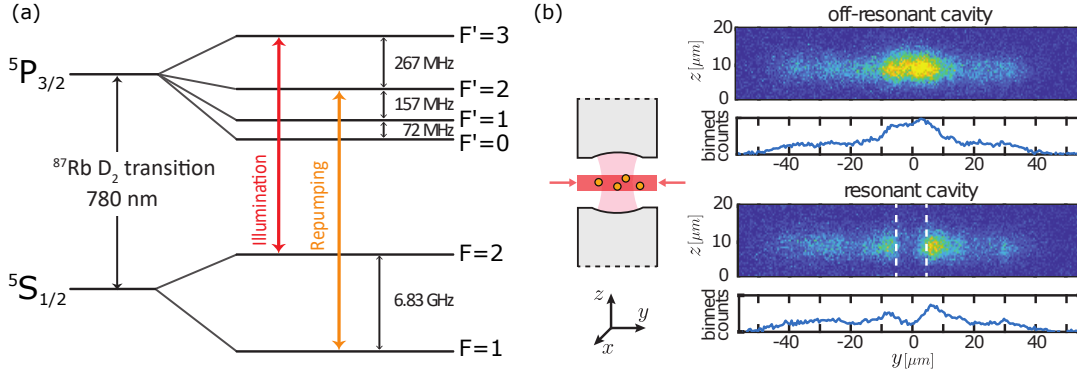


Figure 2.1: **Effect of the cavity on the free space scattering of the atoms when imaging in the ^{87}Rb D2 line.** (a) Scheme of the energy levels. (b) Fluorescence images of the atoms trapped in the optical lattice, averaged over many shots, showing the difference when the cavity is off-resonant and when on resonance with the D2 line (figure extracted from [20]).

2.1 Overview of the imaging technique with the D1 line

As already introduced, the idea to solve the imaging problem was to use the D1 line of Rubidium 87 for the fluorescence detection of the atoms, instead of the previously used D2 line, while keeping the cavity resonant with the latter. In the following I will present this new imaging scheme that was implemented in the main experiment.

2.1.1 Illumination scheme

The energy levels of the D1 line of ^{87}Rb are shown in Figure 2.2a [30]. The ground state $5S_{1/2}$ and the excited state $5P_{1/2}$ have an energy difference corresponding to a wavelength of ≈ 795 nm. Both ground and excited states are subdivided into two hyperfine levels, with $F = \{1, 2\}$ separated by ≈ 6.8 GHz, and $F' = \{1, 2\}$ by ≈ 814 MHz respectively.

In contrast to the D2 line, in the D1 line all four $F \rightarrow F'$ transitions are allowed by electric dipole interaction with similar strength factors. This means that there is no cycling transition possible, like the $\{2 \rightarrow 3\}$ one of the former. Hence, for the imaging process two equally strong lasers are needed for addressing both ground states. Otherwise, if we address only one hyperfine transition, the atom will eventually decay to the other ground level and remain in a dark state insensitive to the illumination.

Having this in mind, there are four different possible combinations $\{F \rightarrow F', F \rightarrow F'\}$ of the transitions addressed simultaneously with two lasers. We consider first the ones where the F' level is shared: $\{1 \rightarrow 1, 2 \rightarrow 1\}$ and $\{1 \rightarrow 2, 2 \rightarrow 2\}$. In these cases, the Λ -scheme of the two optical fields (see Fig. 2.2b) can generate coherent population transfer between the ground levels, and thus inhibit the fluorescence via electromagnetically-induced transparency (EIT) [31], so they should be avoided.

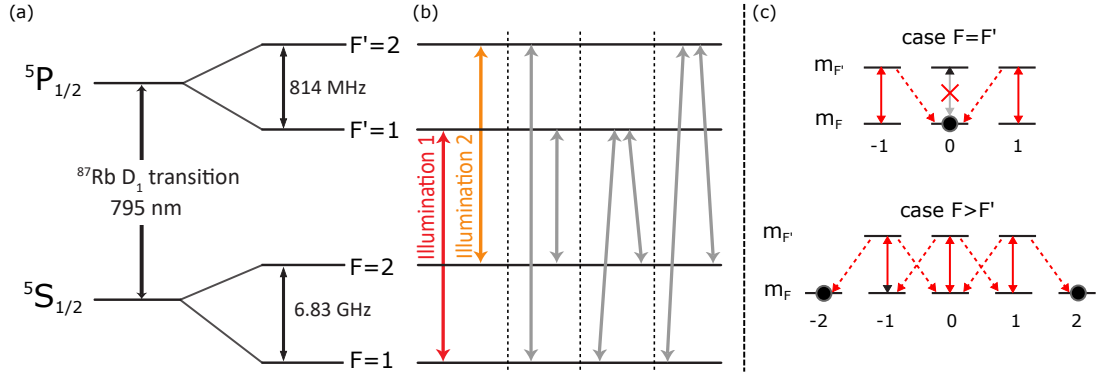


Figure 2.2: **Illumination scheme for imaging in the D1 line of ^{87}Rb .** (a) Schematic of the relevant energy levels. (b) Possible configurations of the two illumination lasers, with the chosen $\{1 \rightarrow 1, 2 \rightarrow 2\}$ for this work. (c) Illustration of the possible cases leading to dark states for linearly polarized illumination.

This leaves us with only two useful illumination schemes: $\{1 \rightarrow 1, 2 \rightarrow 2\}$ and $\{1 \rightarrow 2, 2 \rightarrow 1\}$. Now we have to take into account the allowed m_F transitions withing the hyperfine levels and the resulting dark states (Figure 2.2c), given that our illumination light is linearly polarized. In the case that $F = F'$ the transition $m_F = 0 \rightarrow m_{F'} = 0$ is forbidden, so the state $|F, m_F = 0\rangle$ is dark. Also, if $F > F'$ the two outermost m_F levels are dark as they are not addressed by the illumination fields. Only when $F < F'$ no such states exist. Both choices of the illumination scheme present two dark states that will hinder the fluorescence of the atoms. To circumvent this problem, one can scramble the m_F level by applying a magnetic field misaligned with the polarization axis. Ultimately, for this project we decided to use the illumination scheme $\{1 \rightarrow 1, 2 \rightarrow 2\}$ due to a better performance of our lasers in these transitions (see Section 2.2.2).

2.1.2 Basic theory of fluorescence imaging

In order to have a basic theoretical understanding of the physical processes occurring during the imaging procedure, we start by considering the simplest possible system: a two-level atom illuminated by a monochromatic light source with intensity I and frequency ω_{illu} .

Scattering rate and saturation intensity

This two-level atom will oscillate between excited state $|e\rangle$ and ground state $|g\rangle$, by absorbing photons from the illumination field, and emit photons with the transition energy between the two levels (frequency ω_0). The photon scattering rate R_{sc} is obtained from the steady-state solutions of the optical Bloch equations in an atomic ensemble [32, Ch. 2]:

$$R_{sc} = \frac{\Gamma}{2} \frac{I/I_s}{1 + I/I_s + (2\Delta/\Gamma)^2} \quad (2.1)$$

where Γ is the natural decay rate of the atom from the excited level, $\Delta = \omega_{\text{illu}} - \omega_0$ is the frequency detuning of the illumination frequency from the resonance, and I_s is the saturation intensity of the transition. The latter is defined as the on-resonance intensity at which, in steady-state, the average population of the excited state is $\rho_{ee} = 1/4$.

Equation 2.1 shows that scattering rate exhibits a non-linear response to the illumination intensity. At low driving power, $I/I_s \ll 1$, the behavior is approximately linear and the ensemble population occupies mostly the ground level $|g\rangle$. However, at very high intensities, with $I/I_s \gg 1$, the scattering rate saturates at the asymptotic value of $R_{sc} = \Gamma/2$ and the population of the excited state $|e\rangle$ reaches the maximum $\rho_{ee} = 1/2$.

A quantitative calculation of I_s for a specific transition can be done considering the dipole matrix elements $\langle g|\boldsymbol{\varepsilon} \cdot \mathbf{d}|e\rangle$, with the expression [33]

$$I_s = \frac{c\epsilon_0\Gamma^2\hbar^2}{4|\langle g|\hat{\boldsymbol{\varepsilon}} \cdot \mathbf{d}|e\rangle|^2} \quad (2.2)$$

where $\hat{\boldsymbol{\varepsilon}}$ denotes the unit polarization vector of the electric field.

For illumination light with linear polarization (i.e. $\hat{\boldsymbol{\varepsilon}} = \hat{z}$), an effective saturation intensity for the D1 line of ^{87}Rb ($J = 1/2 \rightarrow J' = 1/2$ transition), without resolving the hyperfine levels, was calculated in ref. [30]:

$$I_{s,(eff,D_1)} \approx 4.5 \text{ mW/cm}^2 . \quad (2.3)$$

Now, when addressing the hyperfine transitions individually, effective dipole moments can be calculated from the one of the encompassing $J \rightarrow J'$ transition [33]:

$$|\langle g|\hat{\boldsymbol{\varepsilon}} \cdot \mathbf{d}|e\rangle|^2 = \frac{|\langle J||\mathbf{d}||J'\rangle|^2}{3} S_{FF'} , \quad (2.4)$$

where $S_{FF'}$ are the hyperfine transition strength factors defined in the reference. Thus, we compute the saturation intensities involved in our imaging scheme, shown in Table 2.1, as

$$I_{s,FF'} = I_{s,(eff,D_1)} S_{FF'} . \quad (2.5)$$

Photon recoil heating

During the process of fluorescence imaging with near-resonant light with wavelength $\lambda = \frac{2\pi}{k}$, a two level atom experiences momentum kicks of magnitude $\hbar k$ when absorbing and emitting photons. In fact, the atom undergoes a random walk where every two steps are generated by each absorption-emission cycle, that results in a heating effect. In our setup, due to the lack of 3D cooling during the imaging process, this heating leads to

Hyperfine transition $F \rightarrow F'$	Strength factor $S_{FF'}$	$I_{s,FF'}$ [mW/cm ²]
1 \rightarrow 1	1/6	0.7479
1 \rightarrow 2	5/6	3.7397
2 \rightarrow 1	1/2	2.2438
2 \rightarrow 2	1/2	2.2438

Table 2.1: Saturation intensities of the D1 line hyperfine transitions calculated from Eq. 2.5 [30, 33].

losses of the atoms from the dipole trap.

For a rough quantitative estimation, we consider that, on average, each scattering event increases the kinetic energy of the atom by an amount comparable to two times the recoil energy [34] $\Delta E_{sc} \approx 2k_B T_r = \frac{(\hbar k)^2}{m_A}$, where T_r is the recoil temperature, and m_A the mass of the atom. We further make the approximation that the atom escapes from the dipole trap if its average energy overcomes the ground state dipole trap depth U_0 [28]. In other words, without cooling, it will be lost after scattering $N_{\text{heat}} = U_0/\Delta E_{sc}$ photons. For the D1 line of ^{87}Rb $T_r = 349$ nK [30], and with the limiting depth of our trap $U_0 = k_B \times 0.5$ mK, the critical number of event is $N_{\text{heat}} \approx 700$, from which we expect to detect $< 2\%$ [28]. Therefore, on average only 14 photons per atom will contribute to the imaging process.

2.2 Experimental setup for imaging using the D1 line

In this section I will describe the technical steps we followed to build, prepare and characterize the different modules of the experimental setup needed for the new imaging scheme based on the D1 line of ^{87}Rb . In the first place, we need sources of coherent light to illuminate the atoms and generate fluorescence. For this to work, the emission frequency of these sources has to be precisely stabilized to address the transitions of the D1 line. Additionally, we need the flexibility to control independently the illumination frequencies and intensities. This degrees of freedom are essential for the optimization of the imaging scheme, as will be shown in Section 2.3. Also, the optical system that collects the fluorescence photons has to be optimized to the D1 line wavelength of 795 nm.

2.2.1 Light sources for the illumination beams

As light sources for our imaging beams we built two external-cavity diode lasers (ECDL) in the Littrow configuration, following the design from refs. [35, 36]. In this particular layout (see figure 2.3), the output of the laser diode impinges on a Littrow blazed grating at an angle close to the design *blaze angle*, such that the first diffraction order is reflected back into the diode and creates the optical feedback needed to select a specific wavelength, and the extended cavity narrows down the broad linewidth of the diode

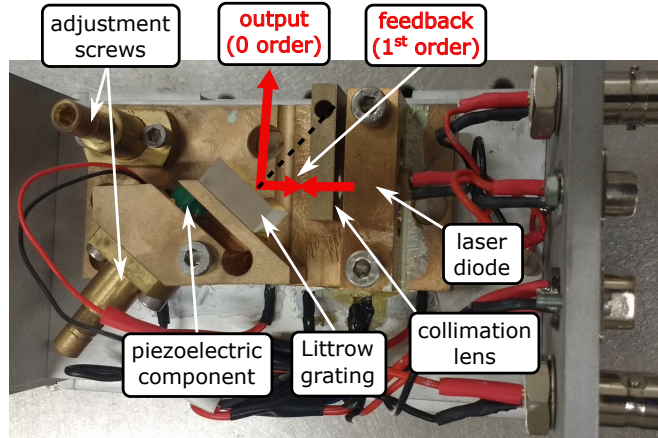


Figure 2.3: Grating laser picture

[37]. Then, the zero order is used as the output of the laser. It follows also that the frequency component fed-back from the grating is directly proportional to the incidence angle. This allows to tune the laser emission frequency by horizontally tilting the grating mount with the corresponding micrometer-screw. Another micrometer-screw changes the vertical angle to optimize the feedback, and thus reduce the threshold current and ensure single mode operation. Additionally, a piezoelectric component placed between the frequency-tuning screw and the grating mount, is used for fine-tuning and linear modulation of the wavelength proportional to the input voltage. In addition, the lasing frequency is also dependent on the driving current and the temperature of the diode, and can be used for tuning as well. The temperature is actively stabilized to a selected setpoint, with a servo controller driving the two Peltier elements located below the main base-plate, inside the casing.

Since it was uncertain if this D1 imaging scheme would work because of the presence of possible dark states, for the proof of principle we decided to use laser diodes¹ available in the lab, with a free-running central wavelength of 785 nm, and a broad spectrum going from 775 to 795 nm. We adjusted our two lasers to the wavelength of the D1 line (~ 794.97 nm) by iterative angle-tuning and feedback optimization, as described above. However, it was particularly challenging to reach the proper frequency in a mode-hop free regime, under normal temperature and current settings. This was mainly because the frequencies at the edge of the emission spectrum exhibit a very low gain, and thus a competition of modes occur. We found an acceptable operating regime when increasing the temperature to ~ 50 °C and at relatively low currents of ~ 50 A. Clear disadvantages of these operating settings are a high sensitivity to temperature fluctuation, and a low output power of the lasers.

¹ Thorlabs L785P090.

2.2.2 Stabilization of the laser frequencies with polarization spectroscopy

For having a consistent and reproducible imaging process, it is fundamental that each illumination laser (IL) emits at a selected frequency, and remains stable over long times. ECDL are sensitive to mechanical perturbations that are always present in a laboratory and to thermal fluctuations, which produce drifts in the emission wavelength. Therefore, it is necessary actively stabilize the lasers by *locking* each one to a chosen atomic transition, using a spectroscopic signal as reference.

From the many techniques developed over the recent years to create useful signals for frequency locking [38], we used doppler-free polarization spectroscopy, first proposed by C Wieman and T. Hänsch in 1976 [39]. This technique is very similar to saturation spectroscopy [38]. But instead of measuring the reduction of absorption of a probe beam by the sample, caused by the saturation with a pump beam, this spectroscopy monitors the change of the probe polarization due optical anisotropy of the medium, induced by optical pumping.

However, we implemented a modification introduced by [40], consisting in using a polarizing beam splitter and two detectors as polarimeter, instead of the original approach of two crossed polarizers and one detector. This improves the sensitivity and the SNR by an order of magnitude.

Basic principle of polarization spectroscopy

The basic principle can be understood as follows (see Fig. 2.4a) [38, 39, 40]: a weak monochromatic *probe* beam crosses a glass cell with the atomic sample, on resonance with one of the atomic transitions, after which its polarization is measured with the polarimeter, consisting of a polarizing beam splitting cube (PBS) acting as analyzer and two photo-diodes, one in each arm of the PBS. Before the cell, such polarization is prepared linear with a angle $\theta = 45^\circ$ with respect to the PBS. Then, for the probe interacting alone with the sample, the intensities of the vertical and horizontal components measured by the detectors are $I_x = I_y = I_0/2$, where I_0 is the total intensity of the beam. The probe can also be described in the circular base as a balanced combination of σ^+ and σ^- polarized light, with a relative phase shift that results in the angle of the linear polarization plane.

Now, a strong *pump* beam with circular polarization (say σ^+), coming from the same laser, is added such that it crosses the probe inside the cell with counter-propagating direction. The effect of this beam is to saturate the transitions of the atoms obeying the selection rule $\delta m = +1$ (σ^+ -driven), depleting in an asymmetric way the different sublevels of the ground state. The influence of the now polarized atoms is to induce a difference, in the absorption coefficient $\Delta\alpha = \alpha_+ - \alpha_-$, as well as in the refractive index $\Delta n = n_+ - n_-$, for the two components of the probe. This corresponds to an effective birefringence of the medium, that rotates the plane of linear polarization of the probe

and thus is detected in the polarimeter.

The polarization signal is obtained by subtracting the measured signals of the two detectors. It has a zero background and is proportional to rotations of the probe polarization plane by an angle $\Delta\theta$, as $I_{\text{signal}} = I_x - I_y = 2I_0\Delta\theta$. When scanning the laser frequency over the resonance, neglecting the birefringence of the glass cell, for $\theta \approx \pi/4$ the approximated shape of the signal has the form [40]

$$I_{\text{signal}} \approx -I_0 e^{-\alpha L} \left(L \Delta\alpha_0 \frac{x}{1+x^2} \right) \quad (2.6)$$

where L is the length of the cell, $\alpha = \frac{1}{2}(\alpha_+ - \alpha_-)$ the normal absorption coefficient, $\Delta\alpha_0$ the maximum absorption difference on resonance, and $x = \frac{\omega_0 - \omega}{\Gamma/2}$ is the rescaled detuning with Γ the power broadened linewidth. This resulting signal has a dispersive shape with zero background, hence it very convenient for using as an error signal for laser stabilization.

Our compact double-spectroscopy setup

Additionally, we used the alternative retro-reflection scheme suggested by [41] that allows a very compact system. In this layout, shown in Figure 2.4a, the input laser is used as the *pump* beam, circularly polarized by a quarter-wave-plate rotated 45° from the axis of the input linear polarization. It is transmitted through a non-polarizing beam splitter and then through a rubidium vapor cell. After the cell, the beam is retro-reflected and crosses a linear polarizer rotated 45° to generate the *probe* beam, that overlaps with the pump. Finally the beams are separated in the beam splitter and the probe is sent to the polarimeter that measures the signal described above. The perfect overlap of pump and probe beams in this layout has the advantage of reducing the Doppler broadening of the signal, caused by a finite crossing angle.

Now, in our case each illumination laser needs its own spectroscopy for stabilization. We have created a highly compact setup by using a single shared Rb vapor cell to lock the two lasers (Fig. 2.4b). Both beams are collimated, with a waist of ~ 1 mm and a separation inside the cell of ~ 1 cm. To avoid alterations of the signal due to external magnetic fields, the rubidium cell is shielded with mu-metal. Furthermore, the optical elements are mounted on a separated breadboard and the lasers delivered by polarization-maintaining (PM) fibers. This makes the setup transportable and the lasers can be easily exchanged.

For monitoring the atomic spectra, the illumination lasers are scanned in frequency with by applying a voltage ramp to the input of the piezo-transducer (see section 2.2.1). The triangular voltage signals come from home-built lock-boxes in *scan mode*, driven by a common waveform generator at 100 Hz, giving an output with tunable amplitude and offset within a maximum range of pm15 V. The spectroscopic hyperfine-resolved signals described qualitatively by Eq. (2.6), that we obtained for each illumination laser, are

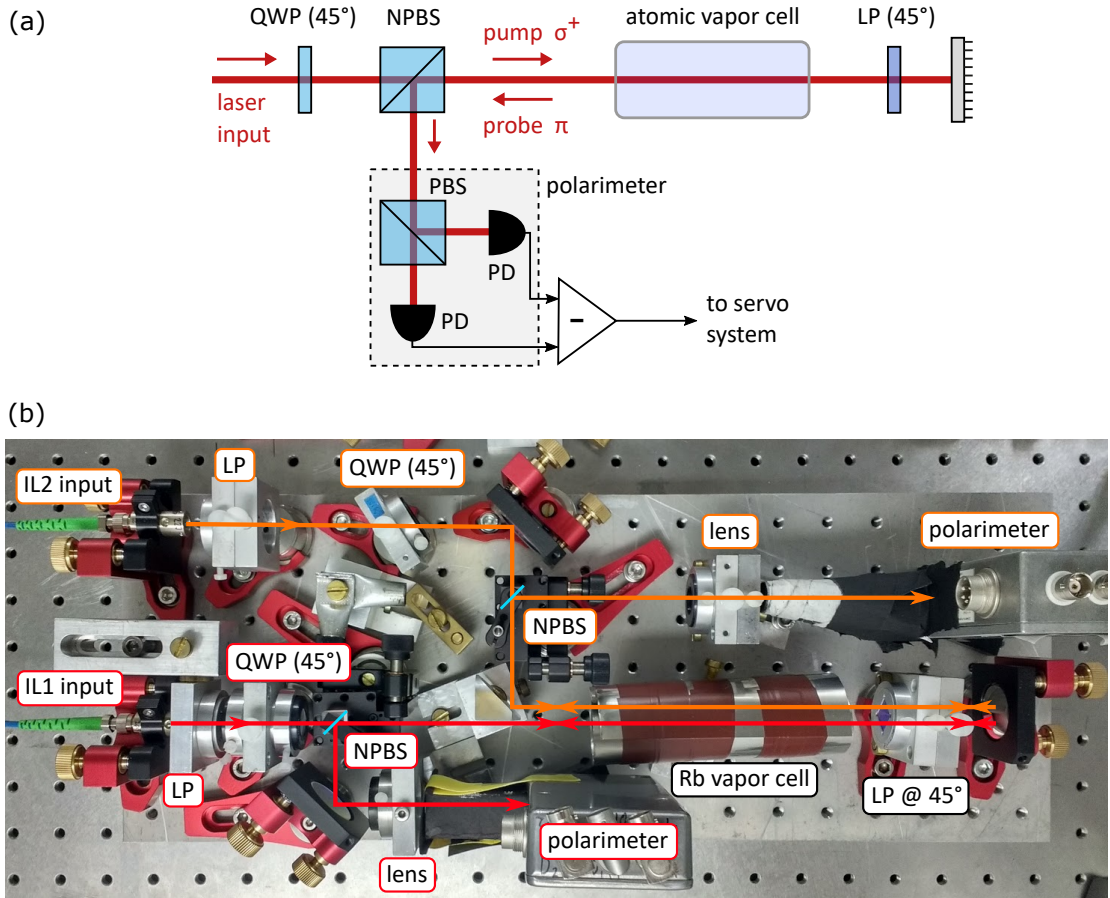


Figure 2.4: **Polarization spectroscopy setup.** (a) Scheme of the retro-reflecting configuration: the pump beam is circularly polarized by a quarter-wave-plate (QWP) rotated 45° from the axis of the input linear polarization. After traversing a rubidium vapor cell, the beam is retro-reflected and crosses a linear polarizer (LP) rotated 45° to generate the probe beam, that overlaps with the pump. The beams are separated with a non-polarizing beam splitter NPBS and the probe is sent to the polarimeter, consisting of a polarizing beam splitter (PBS) acting as analyzer and two photo-diodes (PD), one in each arm of the PBS. (b) Our compact spectroscopy setup built to lock both illumination lasers to the same Rb vapor cell: the mounting on a separated breadboard and the fiber-coupled inputs from the illumination lasers (IL1 and IL2), make it portable and adaptable to exchange of the lasers.

depicted in Figure 2.5, together with the respective absorption spectrum. For stabilizing the lasers, each polarization signal is fed to the respective lock-box and used as error signal after being amplified.

At this point, each laser can be locked to any of the two ^{87}Rb D1 hyperfine transitions of its respective spectrum. From the two configurations that are useful, we decided to address the transitions $\{1 \rightarrow 1 \text{ and } 2 \rightarrow 2\}$, as discussed in Section 2.1.1.

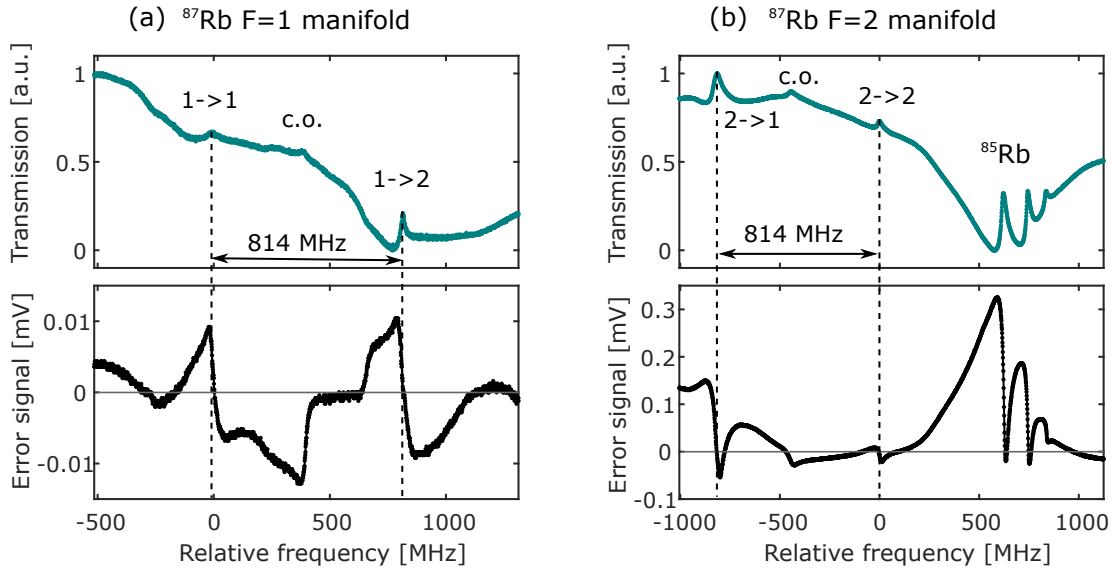


Figure 2.5: **Polarization spectroscopy signals of the D1 line of ^{87}Rb , and the respective absorption spectrum, obtained for each illumination laser (IL).** (a) Spectrum for IL1, only the ^{87}Rb $F = 1 \rightarrow F' = \{1, 2\}$ manifold is visible. (b) Spectrum for IL2, the ^{87}Rb transitions in the $F = 2 \rightarrow F' = \{1, 2\}$ manifold can be seen, as well as some transitions that belong to ^{85}Rb . Also the expected crossover (c.o.) peak appears between each couple of transitions with the same ground state.

Minimal crosstalk between the two spectroscopy beams was observed when scanning over a broad frequency range, but it was negligible when the scan was reduced, and did not compromise the stability of any of the two locks. Nevertheless, when looking at the resulting signals, it is noticeable that the peak-to-peak amplitude for all ^{87}Rb D1 transitions, is small compared to the maximum features obtained typically for the D2 line [40]. This is due principally to two factors: on the one side the limited power of our lasers does not allow to fully saturate the atoms with the pump beam. On the other hand, the absence of closed transitions for the D1 line leads to hyperfine pumping to the second ground state, from both the pump and the probe, thus decreasing the overall absorption [42]. The latter can be improved by heating the atomic vapor cell to decrease the transient time of the atoms across the beam (presently at room temperature), and by reducing the power of the probe to $\sim 0.001I_{sat}$ [43]. However, the signals without further optimization were sufficient for stabilizing the lasers and testing the imaging scheme, as will be shown in section 2.3.

2.2.3 Frequency shifting setup

Once the emission frequencies of our illumination lasers are stable, we scan the frequency of the beams sent to the main experiment with respect to the locking setpoint. This

gives us a necessary degree of freedom for the imaging system, that allows, for instance, to optimize the detuning between illumination and atomic resonance, and also, as we will see in Sec. 2.3.2, a fast switching mechanism.

For this purpose we used the setup shown in Figure 2.6. First, each laser beam is split into one arm that feeds the spectroscopy, and another that is used for illumination. Both illumination beams are then combined and coupled to a same PM fiber, to clean and overlap their modes. A linear polarizer before the fiber in-coupler mixes the polarizations (that would be orthogonal without it), and an additional half-wave-plate polarizer can be rotated to balance the intensity proportion between the two frequency component of the joint illumination beam.

After the fiber, the beam goes through two acousto-optic modulators, both in double pass configuration, which shift the frequency of the illumination beam. The first modulator (AOM1) is coupled to the -1^{st} order and is used to scan the frequency and as a switch for the beam. The second modulator (AOM2), coupled to the $+1^{st}$ order and operated with constant RF frequency, sets the center frequency of the scan by partially compensating the central shift induced by AOM1. In this configuration, it is possible to scan the frequency of the beam by $\sim \pm 50$ MHz, and shift the offset of the center frequency from the resonance by $\sim \pm 40$ MHz. Besides, the intensity of the illumination beam is actively stabilized: after the frequency scanning setup, a monitoring photodiode detects deviations from the setpoint intensity that are compensated with a servo system acting on the AOM1 RF power. Finally, the beam is split into the two illumination arms, with balanced intensities and orthogonal linear polarizations, that are fed to the experiment to illuminate the atoms inside the cavity from counter-propagating directions.

2.2.4 Optimization of the optical imaging system

The optical system used to image the atoms can be seen in the diagram of the main experimental setup in Chapter 1 (Figure 1.2). During the imaging process, the fluorescence is collected by one of the high-NA aspheric lenses² that surround the fiber cavity, with their focal point at the center of the 3D dipole trap (recall the description of the main experimental setup in Ch. 1 and [20]). Then, the collected light is separated from the outgoing dipole trap beam by a dichroic mirror at 45° , and later focused by a plano-convex lens³, to form the image of the atoms on the sensor of the EMCCD camera⁴. This long focal distance lens is mounted on a translation stage for focusing optimization. The focal length of the focusing lens was chosen to give a magnification factor $M \approx 35$ [28], such that the point spread function (PSF) of an atom is imaged onto ≥ 2 pixels, this having been demonstrated to maximize the SNR without information loss [44]. Also, previously, a plano-concave compensation lens⁵ had been added after the dichroic mirror

² Lightpath 352240, $NA = 0.5$, $f_{eff} = 8$ mm, $D = 10$ mm [28, 20]

³ $f = 300$ mm, $D = 50.8$ mm.

⁴ Andor technology, Ixon 3 DU-897-BV, with 512×512 pixels of $16 \mu\text{m} \times 16 \mu\text{m}$.

⁵ $f = -1000$ mm, $D = 50.8$ mm

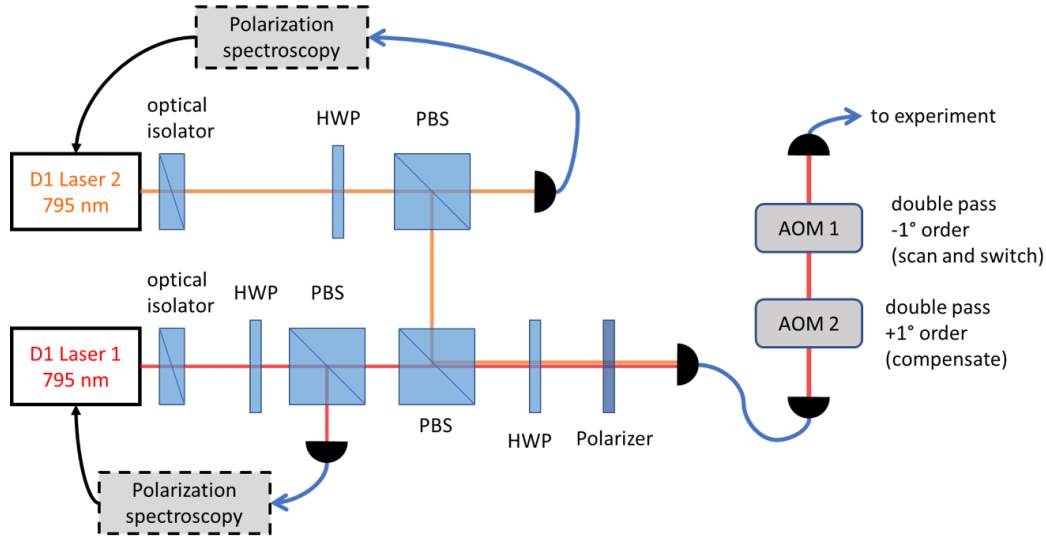


Figure 2.6: **Setup for frequency scanning and intensity stabilization of the illumination beam.** Each laser beam is split with a half-wave-plate (HWP) plus a polarizing beam splitter (PBS) into one arm for the spectroscopy, and another for the illumination. The illumination beams of both lasers are combined with a PBS, their polarization mixed with a rotated polarizer, and coupled to a same PM fiber for mode-overlap. A HWP before the polarizer is used to balance the intensity of the two frequency components of the beam. Two double-pass AOMs are used to shift the frequency of the beam: AOM1 acts as a switch and scans $\sim \pm 50$ MHz, while AOM2 shifts the offset of the center frequency by $\sim \pm 40$ MHz.

to correct a slight convergence of the beam, due to a small displacement of the trapping plane from the focal plane of the high-NA lens.

When migrating to the imaging scheme in the D1 line, a number of adjustments were needed to account for the change of the fluorescence frequency. We simulated our system to optimize it for the new wavelength using the optical design software OSLO⁶. Due to the different chromatic aberrations of the aspheric lens for $\lambda = 780$ nm and $\lambda = 795$ nm, it was necessary to change the focal length of the compensation lens⁷. The new optimal positions of the compensation and focusing lenses were also optimized with OSLO, achieving a theoretical peak Strehl ratio of 0.966 and a magnification factor of $M = 49.4$. Lastly, new band-pass interference filters⁸ were placed in front of the EMCCD camera to restrict the optical access to only D1 light. After the changes, the final adjustment of the focusing are made actively while taking pictures of the atoms. This and the experimental determination of the magnification factor are shown in the next section.

⁶ OSLO Optics, Lambda Research Co., <http://lambdaresearch.com/oslo/>.

⁷ $f = -2000$ mm, $D = 50.8$ mm

⁸ AHF Analysentechnik F97-794 and Thorlabs FB800-10

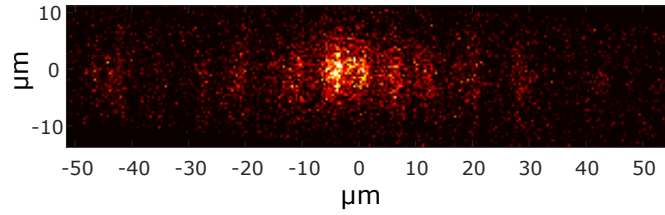


Figure 2.7: Example of a fluorescence image of the atoms trapped in the optical lattice, taken with an exposure of 100 ms, illumination frequency shift from free space resonance ≈ 44 MHz and intensity ≈ 152 mW/cm².

2.3 Results and characterization of the new imaging scheme

For all the measurements presented in this section, the illumination lasers were locked to the D1 transitions $F = 1 \rightarrow F' = 1$ and $F = 2 \rightarrow F' = 2$. Both lasers with the same power had equal intensity in the counter-propagating arms of the illumination beam. The waist of the beams at the atoms position is $w_0 \approx 13$ μm. The electronic multiplication gain of the EMCCD camera was set to 300.

As already mentioned before, the focusing was adjusted to obtain sharp images. Then, to characterize the system and find a regime for good imaging we performed the following measurements: first we determined the new magnification factor of our imaging system; then we investigated the effect of the fluorescence when changing the illumination frequency and intensity.

An example of the images we obtained with an exposure time of 100 ms, and illumination intensity in each transition ≈ 152 mW/cm², and the frequency shift from the free space resonance of the atoms ≈ 44 MHz, is shown in Figure 2.7. In the image, the pattern of the dipole trap can be observed, as well as the region of overlap of the 3D optical lattice inside the cavity, evident as a brighter area because of the higher survival probability of the atoms, given the destructive nature of our imaging scheme.

2.3.1 Calibration of the magnification factor

Since we moved the position of the focusing lens to optimize the sharpness of the images at the new fluorescence wavelength, we expect that the magnification factor changed. Hence, we calibrate the magnification factor of our imaging system, with a new technique. The usual method to determine the magnification is finding the average distribution of atoms position to extract the lattice spacing [45, 27, 28]. This, however, requires very long measurement times and high signal-to-noise images, that we can not have due to the lack of a cooling mechanism. Therefore, we implemented a novel way of measuring this factor. This method is necessary in our case since it is not sensitive to losses, nor to atom hopping (assuming that hopping occurs to both directions of the lattice with the same probability).

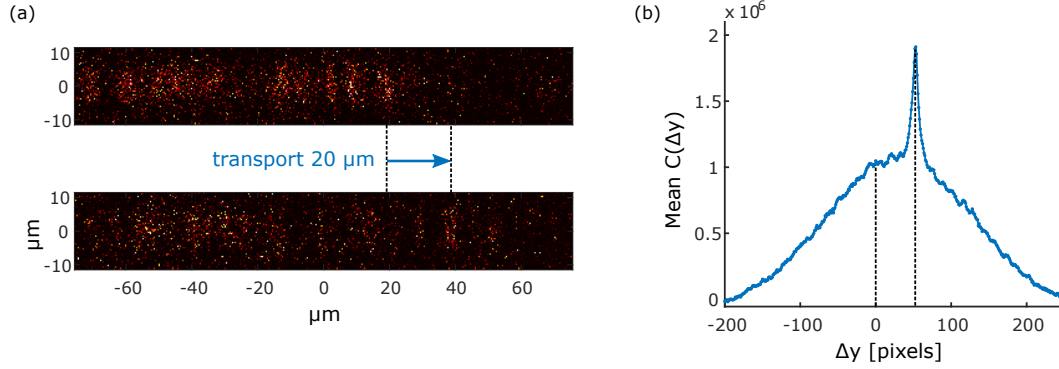


Figure 2.8: **Novel technique to calibrate the magnification factor.** (a) Two images of the atoms are taken with a lateral transport of $20 \mu\text{m}$ between the two shots. (b) The mean of the cross-correlations $C(\Delta y)$ of many shots before and after the transport, show a distinct peak for a shift between the signals $\Delta y = 53$ pixels, that correspond to the transport distance.

We load a few atoms in the 3D lattice and take two pictures. The first one directly after the loading, and the second one after transporting the a distance $D_{\text{object}} = 20 \mu\text{m}$ with the conveyor belt, as seen in Figure 2.8a. Next, we integrate the counts of each image in the perpendicular direction to the dipole trap, to obtain signals of fluorescence versus position in the trap $S(y)$ (in pixels), and finally calculate the cross-correlation of the reference signal S_r with the one after the transport S_t , defined as

$$C(\Delta y) = \sum_{y=-\text{inf}}^{\text{inf}} S_r(y) S_t(y + \Delta y) \quad (2.7)$$

where Δy is the induced shift in pixels between the two signals.

As the cross-correlation is a measure of the similarity between two signals as a function of their relative shift (in this case in pixels), a peak is expected when the shift corresponds to the transport distance in the image D_{image} . The magnification is calculated as $M = \frac{D_{\text{image}}}{D_{\text{object}}}$. When repeating this procedure for many shots, averaging the computed cross-correlations, we obtained the values $C(\Delta y)$ plotted in Figure 2.8b as a function of the shift Δy . A distinct peak is found for a shift of 53 pixels, corresponding to the $20 \mu\text{m}$ of the transport. The underlying feature comes from the spurious coincidences with the counts from other atoms or from the background. Considering the size of the pixels of $16 \mu\text{m}$ per side, the magnification factor is $M = 42.4$ which is slightly higher than the optimum one of $M \approx 35$, but smaller than the predicted one from the design ($M \approx 49$), and still fulfills the condition for a good SNR (see Sec. 2.2.4). We attribute the discrepancy from the expected value to imprecision in the distances of the setup for the simulation with the OSLO software.

2.3.2 Optimization of the illumination frequency and power

Until now we have demonstrated that the new imaging scheme works properly, although we still have the problem of atom loss. It is necessary to find the parameters, in particular the illumination intensity and frequency, that optimize our images. A good imaging requires the highest SNR. From Eq. 2.1 we see that the scattering rate is maximum for zero detuning, and it grows with the illumination intensity, but this does not imply the highest SNR, since photon recoil heating also increases (see Sec. 2.1.2). For this reason it is important to do a systematic characterization of the dependence on the two parameters mentioned above.

Our system is more complicated than for a cycling transition, since we address two transitions with two equally strong lasers at the same time. In this case, the effective scattering rate of the atoms will be related to the rates of the individual addressed transitions (see Appendix A). If one of the rates dominates, we find that the effective scattering rate will be limited by the slower transition.

The basic experimental sequence to characterize the effects of power and frequency on the fluorescence, starts with loading a few atoms in the overlapping region of the 3D dipole traps. There, an image is taken with the EMCCD camera with an exposure time of 100 ms. During the exposure period, the illumination beams are switched on with specific values of power and frequency. Afterwards, the dipole traps are switched off and a second image is taken to use it for background subtraction. Then, from the corrected image data, we obtain a measure of the average fluorescence of the atoms by integrating the CCD counts in the cavity region (Fig. 2.9a). Here we just focus in the region that corresponds to the 3D optical lattice, since this is the relevant region.

Effect of the illumination intensity

We investigate the effect of the illumination intensity on the fluorescence. For this, we performed a 12 points linear ramp of the beam intensity for each transition from $I_{illu} = 50.3$ to 190.1 mW/cm². The frequency detuning from the resonance frequency in free space of both lasers was kept constant at $\omega_{illu} - \omega_{0,fs} = 2\pi \times 44.1$ MHz. For each measurement point of the scan the fluorescence was measured with the basic sequence introduced above and averaged over 100 images.

The results are shown in Figure 2.9b, where we plot the integrated EMCCD counts in the cavity region versus the illumination intensity per transition. We see that the behavior of the fluorescence has two regions. Below an intensity of ~ 100 mW/cm² the relation is approximately linear, which is expected from Eq. 2.1, although above this point the fluorescence saturates. In terms of the saturation intensities of the used hyperfine transitions, given in Table 2.1, this intensity corresponds to $\sim 134I_{sat,11}$ and $\sim 45I_{sat,22}$.

Effect of the illumination frequency

Next, we studied the influence of the illumination frequency on the fluorescence. We used a similar sequence than for the power scan but, in this case, the beam intensity was fixed and we changed linearly the frequency of the illumination beams with 15 points, with values of the free space detuning from $\omega_{\text{illu}} - \omega_{0,\text{fs}} = 2\pi \times -31.2$ MHz to $2\pi \times 74.1$ MHz. For the fluorescence of each frequency point, 200 images were averaged. To check if the effect was different for different intensities, this same scan was performed for the values $I_{\text{illu}} = 32.4, 65.5$ and 131.8 mW/cm².

In Figure 2.9c we report the results of these sequences. For all three values of I_{illu} the plots show an asymmetric curve, with the maximum at a free-space detuning around $\omega_{\text{illu}} - \omega_{0,\text{fs}} = 2\pi \times 45$ MHz. For red detunings the fluorescence decreases as expected. For higher frequencies, we attribute the sharp reduction on the detected fluorescence due to high heating rates and atom losses. This suggest that the AC-Stark shifted resonance could be at ~ 65 MHz. However, we are addressing several m_F states during the imaging process and this value can represent an average of all the existing shifts. To precisely measure the shift is complicated since there is no closed transition for the D1 line and therefore, a mixture of Zeeman states will always be present. A more elaborated experiment is then needed, which goes beyond the scope of this work. A surprising result is the absence of power broadening at the resonance, that is expected for such high powers. This still has to be investigated.

2.4 Conclusions and next steps

In this chapter we studied the fluorescence imaging of atoms with the D1 line, as an alternative to the D2 line imaging that had undesired effects from the cavity interaction. The behavior with respect to the illumination parameters of frequency and intensity was investigated, and a regime for good imaging was found.

Yet, to find the optimum illumination intensity, one would need to have the complete perspective of the trade-off between fluorescence and lifetime. For this, we would need to perform lifetime measurements, cooling measurements and histogram measurements of the atom number [28]. However such a detailed characterization is very lab-time consuming and were not the priority at the present time. We also identified that at a frequency $\omega_{\text{illu}} - \omega_{0,\text{fs}} = 2\pi \times 45$ MHz the fluorescence is maximum, but this might not correspond to the highest SNR. To find the optimum value it is necessary to measure the survival probability of the atoms in the trap.

Furthermore, a novel technique for the characterization of the magnification factor was

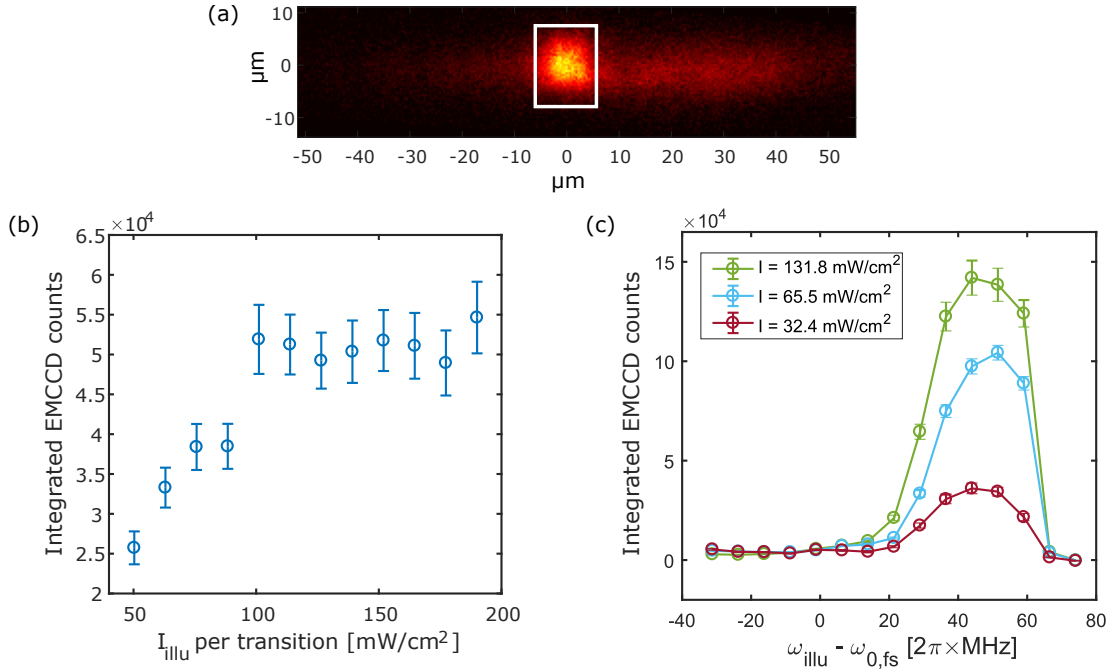


Figure 2.9: **Characterization of the D1 imaging method with respect to the illumination parameters.** (a) Example fluorescence image of the atoms for one of the measurement points, averaged over ≈ 100 shots. The counts are then integrated in the region of the 3D lattice marked in white. (b) Effect of the illumination power on the integrated fluorescence. (c) Effect of the illumination frequency on the integrated fluorescence. The error bars were calculated as the standard deviation of the gaussian mean of the sample.

shown, with the advantage of being robust and precise even with very low statistics. Also it is insensitive to partial atom loss and hopping. This technique could potentially be used to extract information about the PSF of the atoms from the width of the cross-correlation peak. This could allow, for example, for a very precise fast optimization of the focussing of an imaging system.

Still an important challenge that needs to be faced is the implementation of a cooling mechanism simultaneous to the imaging. In principle, it is now possible to combine the imaging in the D1 line with cooling schemes in the D2 line, for instance 2D molasses or Raman cooling that has already been used in the group [46].

The measurements presented in this chapter show that it is possible to obtain images using the D1 line and provide a good starting point for further optimization of this imaging technique.

Optical addressing of atoms in an optical lattice

For many experimental applications with few localized atoms, the ability to manipulate them individually has become an important requirement. In this regards, schemes for addressing single atoms in optical lattices have been implemented in a variety of ways. For instance, with a focused beam in very long wavelength CO₂-laser lattices [47], or by making the resonance frequency of the atoms position-dependent with a strong magnetic field gradient [48]. In another approach, an electron beam was used to push out single atoms from a 2D lattice to form arbitrary patterns [49]. More recently, steered tightly focused laser beams were used to shift the energy levels of target atoms such that they are individually on resonance with global addressing fields [50, 51]. Furthermore, similar steerable focused beams have been used as push-out beams to eliminate unwanted atoms from a probabilistic sample [52], as well as to assemble arrays of atoms trapped in independently controllable dipole traps [53].

Having a robust imaging technique for atom localization at hand, an addressing scheme is needed to handle the second experimental condition for the two-atom dissipative entanglement protocol [9, 10], explained in Chapter 1: to control the number of atoms and their relative distance inside the cavity mode. The condition is such that a $e^{-i\pi} = -1$ phase difference in the driving field between the two atoms is needed. For this, their relative distance has to be $\Delta y = (2n + 1)\lambda/2$, e.g. an odd number of lattice sites. Our approach to fulfill this condition is to perform a high probabilistic loading of atoms inside the 3D optical lattice, and to prepare the desired atom pattern in real-time by selectively pushing the unwanted atoms out of the trap with a steerable addressing beam.

The second part of my Master project was the implementation of this addressing system. It will be presented in the following chapter, which is divided in two sections. In the first part, the techniques and modules that compose the addressing setup are described and explained. Then, in the second section, I present the results of the characterization and the optimization of the push-out process.

3.1 Implementation of the addressing system

The addressing setup we implemented for position-selective push-out of atoms is shown in Figure 3.1 in a simplified form. Images of the atoms trapped in the optical lattice inside the cavity are taken with an EMCCD camera along the x axis (see Chapter 2 for a detailed explanation of the imaging technique). The fluorescence signal is processed by an algorithm, developed in the past in our group [27], that determines the position of the atoms in the lattice with sub-pixel resolution in a few milliseconds [54].

Once the positions are known, a strongly focused resonant beam can be used to expel atoms from defined lattice sites. This addressing beam is aligned along the x -axis dipole trap, overlapping in part with the imaging system, and is finally focused on the optical lattice by the same high-NA lens used for the imaging. The push-out beam is steered to the aimed positions by a 2D acousto-optic deflector, which creates an angular deflection from the x -axis as a function of the frequency of an RF driving signal. This deflection is then converted into a longitudinal displacement on the yz -plane of the lattice via an optical transfer system. Additionally, an acousto-optic modulator, preceding the deflector, is used to compensate the frequency shift induced by the AOD and to stabilize its intensity for consistency of the push-out process.

A straightforward application of a 2D addressing system, is the generation of arbitrary patterns of atoms with defined number and spacing in the yz imaging plane. The resulting pattern can be later shifted using the the optical conveyor belt along the y -axis.

In the following, I will first give an overview of the push-out technique, and then explain in detail the two relevant modules that compose the addressing setup, that is, the acousto-optic deflector and the optical transfer system.

3.1.1 The push-out technique

The push-out technique was developed previously in our group for state selective detection of atoms [55]. In contrast, in our case we use a state-independent push-out to expel the target atoms from the optical lattice. For this, we shine a strongly focused laser with linear polarization, resonant with the D2 line of ^{87}Rb atoms in the cycling transition $F = 2 \rightarrow F' = 3$. The beam also contains repumping light resonant with the $F = 1 \rightarrow F' = 2$ to address the $F = 1$ ground state and avoid dark states. The combination of transitions induces a highly efficient scattering of photons, which causes recoil heating to the point where the motional energy of the atoms exceeds the trap depth U_0 and escapes. The addressing beam is aligned perpendicular to the yz -plane of the lattice.

Here we must differentiate two regimes. At high intensities, if the radiation pressure from the push-out beam is stronger than the radial dipole force, an atom absorbs enough photons to escape in less than half the oscillation period of the trap. In this case the

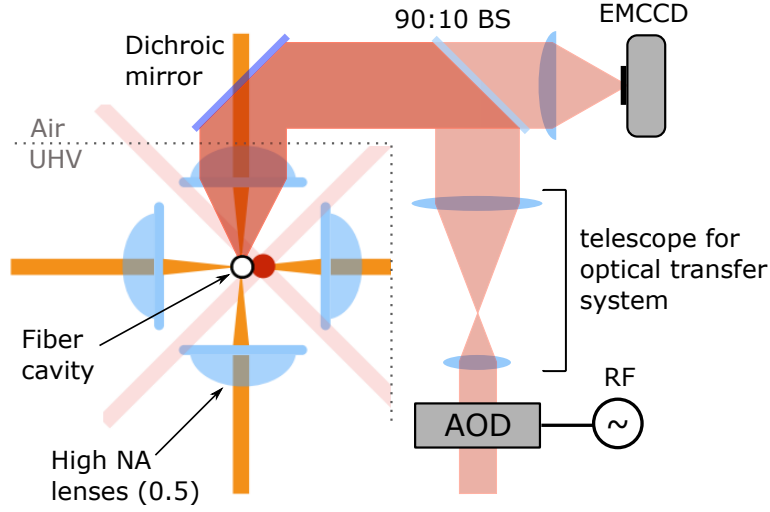


Figure 3.1: **The addressing scheme.** The push-out beam is directed to the target atoms by an acousto-optic deflector via an optical transfer system, and focused on the optical lattice yz -plane with one of the high-NA lenses.

photon momenta are linearly summed and the atom is *pushed* out of the trap after absorbing $N_{\text{push}} = \frac{\sqrt{2m_A U_0}}{\hbar k}$ photons. On the contrary, if the radiation pressure is smaller than the trapping force, photon recoil heating is the dominant effect (discussed already in Section 2.1.2) and the atom is *heated* out of the trap in $N_{\text{heat}} = \frac{m_A U_0}{\hbar^2 k^2}$ scattering events. Additionally, to increase the efficiency of the push-out process, we lower the trap to $\approx 20\%$ of its initial value.

Mostly interesting for our aim is the difference of efficiency of the two processes [55]; a direct comparison $N_{\text{push}} = \sqrt{2N_{\text{heat}}}$ shows that the push-out is more efficient than the heat-out. This gives us the possibility to find a beam intensity at which the target atoms are pushed out of the lattice, but the neighboring atoms are not yet heated out and prevail. The technique thus allows high efficiency and selectivity that are required properties of any addressing system.

3.1.2 Beam steering with an acousto-optic deflector

The first element of our addressing system is a 2-dimensional acousto-optic deflector (AOD) that permits to control the angular direction of the addressing beam, that is then fed to the optical transfer system. Here I give an overview of the general working principle of AODs, and in particular of the characteristics of the deflector we used.

Working principle of acousto-optic deflectors

The general working principle of an acousto-optic deflector, illustrated in Figure 3.2a, is very similar to the well-known one of the acousto-optic modulator (AOM). A piezoelectric transducer driven by an RF signal vibrates at a frequency f_{RF} , thus creating a sound wave that travels with speed v through a crystal of refractive index n , called Bragg cell. Due to the elasto-optic effect, the sound wave induces a periodic variation of the refractive index in the optical medium. For a laser beam (frequency ν_0 , wavelength in vacuum λ_0) traversing the crystal, this is equivalent to a diffraction grating that generates Bragg scattering when the phase-matching condition between input and output beam and the sound wave is fulfilled. Under this condition the angles of the incident and diffracted beams with respect to the grating normal (θ_i, θ_d) are equal and follow the expression [56]

$$\theta_i = \theta_d \approx \frac{\lambda_0 f_{\text{RF}}}{2n v}. \quad (3.1)$$

Additionally, the optical frequency is Doppler shifted by the acousto-optic interaction, such that the output beam has an order dependent frequency

$$\nu'_0 = \nu_0 + i f_{\text{RF}} \quad (3.2)$$

where $i \in \mathbb{Z}$ denotes the diffraction order.

In contrast to an AOM, for a deflector the most important effect is the dependence of the diffracted angle on the driving acoustic frequency. In this context, a main difference between an AOM and our deflector is that the latter contains a birefringent crystal (TeO_2 [57]) instead of an isotropic medium, allowing to obtain a wider scan range at high efficiency [58]. In this case the optical wave interacts with the slow-shear mode of the acoustic wave and produces anisotropic diffraction. The incident and diffracted angles for perfect phase-matching as a function of the acoustic frequency are governed by Dixon's equations [59]

$$\begin{aligned} \sin \theta_i &= \frac{\lambda_0}{2n_i v} \left[f_{\text{RF}} + \frac{v^2}{f_{\text{RF}} \lambda_0^2} (n_i^2 - n_d^2) \right] \\ \sin \theta_d &= \frac{\lambda_0}{2n_d v} \left[f_{\text{RF}} - \frac{v^2}{f_{\text{RF}} \lambda_0^2} (n_i^2 - n_d^2) \right] \end{aligned} \quad (3.3)$$

with n_i and n_d the refractive index for the incident and diffracted beam respectively, and depend on the cut and alignment of the crystal. A theoretical plot of the nonlinear behavior of these angles versus the acoustic frequency is shown in Figure 3.2b. There is a region around the minimum of θ_i where the incident angle stays almost constant, while the diffraction angle has a quasi-linear dependence $\theta_d \propto f_{\text{RF}}$. This is the region of operation of the AODs since high angular deflection is achieved with a minimum change of the optimum incident angle, and hence with almost no drop in efficiency. The full scan angle of the AOD θ_{AOD} is defined as the difference between maximum and minimum

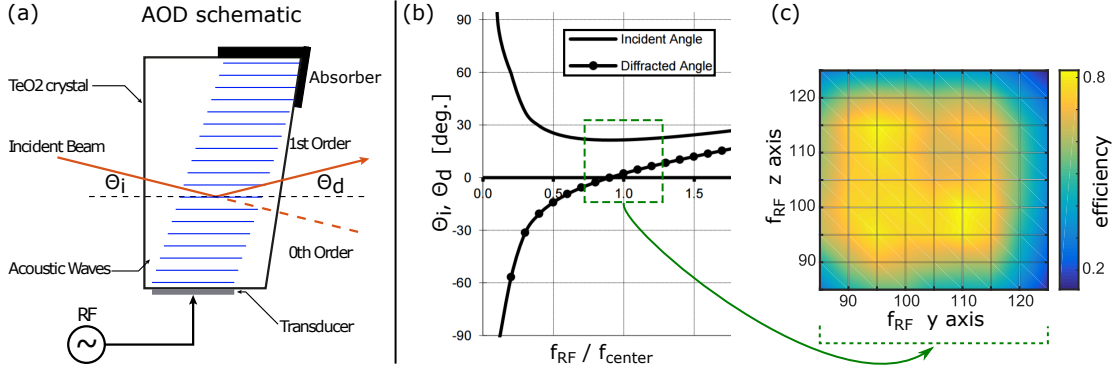


Figure 3.2: **Working principle of an acousto-optic deflector (AOD).** (a) Schematic of an AOD: a piezoelectric transducer driven by an RF signal generates an acoustic wave inside a TeO₂ crystal. The input laser beam incident at angle θ_i is diffracted by the interaction with the sound wave, so the +1st order output beam has an angle θ_d . The main difference with an AOM is the anisotropic diffraction in the birefringent crystal (TeO₂) [59] by coupling with the slow-shear acoustic mode, so $\theta_i \neq \theta_d$ in contrast to the Bragg regime. (b) Theory plot of the dependence of Θ_i and Θ_d on f_{RF} (Eq. 3.3) for perfect phase matching in the case of anisotropic diffraction (source [60]). The green dashed rectangle shows the region of operation of AODs, that allows wide scan angles with high broadband efficiency [58]. (c) Measured diffraction efficiency of the +1st/+1st order of our 2D AOD¹ as a function of the driving RF frequency f_{RF} of both axes y and z .

diffracted angles within its RF bandwidth:

$$\theta_{AOD} = \theta_{d,max} - \theta_{d,min} \propto \frac{\lambda_0 f_{RF}}{2n v}. \quad (3.4)$$

It is also known that the anisotropic acousto-optic effect couples two different polarization modes of the light, thus producing a $\approx 90^\circ$ rotation of the linear polarization of the input beam. Nevertheless, in the case of 2-axis deflectors with an independent Bragg cell for each axis, this effect is compensated by the successive rotations induced by the two crystals.

Our high resolution 2D deflector

In our setup we use a 2D AOD¹ composed by two cross-mounted 1D deflectors, each one controlled by a separate RF driver², thus allowing to deflect the beam along two axes independently. We call y the horizontal axis and z the vertical one, as this will correspond to the alignment when implemented in the main experimental setup.

Each one of the 1D AODs has a central frequency of 104.5 MHz and a bandwidth of 36 MHz. A highlight of the deflector is a wide 2D scan angle with high resolution, since

¹ DTSXY-400-780 from AA-optoelectronic.

² RF driver DRFA10Y-B-0-60.150 and amplifier AMPA-B-34-20.425 from AA-optoelectronic.

in the full deflection range of the yz -plane it can resolve 400×400 points. After a careful characterization before the implementation in the main experiment, we measured for the y -axis a full scan angle of $\theta_{\text{AOD},y} \approx 2.56^\circ$ with a slope of $m_y \approx 0.06^\circ/\text{MHz}$, and for the z -axis $\theta_{\text{AOD},z} \approx 2.77^\circ$ with $m_z \approx 0.07^\circ/\text{MHz}$. We also performed a 2D characterization of the diffraction efficiency as a function of the RF frequency of both axes, plotted in Figure 3.2c. In fact we can see that the efficiency is relatively constant above 70% within almost the full bandwidth of each axis, as expected from the anisotropic diffraction discussed before. Also the response times of the AOD were measured, resulting a dead time of $3.54 \mu\text{s}$ and a rise time of 580 ns .

Furthermore, the deflector is configured in the $+1^{\text{st}}/ +1^{\text{st}}$ order, so the output frequency of the beam is $\nu'_0 = \nu_0 + f_{\text{RF},y} + f_{\text{RF},z}$. Therefore we use an AOM in double pass configuration in the -1^{st} order before the deflector to compensate for the frequency shift and stay on resonance with the atoms.

3.1.3 Optical transfer system

The output beam from the acousto-optic deflector is transformed into the push-out beam using the optical transfer system shown in Figure 3.3. It consists of a telescope, composed of two doublet lenses³ and the high-NA aperture aspherical lens⁴, also used to collect the fluorescence in the imaging system.

We noted previously that imaging and addressing systems have to share part of their optical paths (recall Figure 3.1). For this they are joined with a 90:10 beam splitter (BS) close to the focusing lens of the imaging setup. As a consequence, the only way of not disturbing the imaging system is to place the telescope before the overlap region. In fact, the exchange of the compensation lens of the imaging system (Section 2.2.4) allowed such overlap by ensuring a collimated beam at the joining point.

The main constraint for the design came from the fact that the overlapping BS could only be placed at a distance of $\approx 45 \text{ cm}$ from the high-NA lens, because of the spatial layout of the imaging optics (see Sec. 2.2.4). Consequently, this defined the minimum focal length of the second telescope lens f_2 . After a careful design with the simulation software OSLO⁵, we chose the doublet lenses with $f_1 = 80 \text{ mm}$ and $f_2 = 500 \text{ mm}$ for the telescope. The use of doublet lenses reduces the possible spherical aberrations caused by the off-axis propagation of the deflected beams.

The designed optical transfer system has two simultaneous functions. The first one is to convert the angular deflection $\theta_{\text{AOD}}(\nu_{\text{RF}})$, generated by the AOD, into a linear displacement of the focal point of the push-out beam on the lattice yz -plane. For this,

³ Thorlabs AC254-080-B with $f_1 = 80 \text{ mm}$ and AC508-500-B with $f_2 = 500 \text{ mm}$.

⁴ Lightpath 352240, $NA = 0.5$, $f_{\text{eff}} = 8 \text{ mm}$, $D = 10 \text{ mm}$ [28, 20].

⁵ OSLO Optics, Lambda Research Co., <http://lambdares.com/oslo/>.

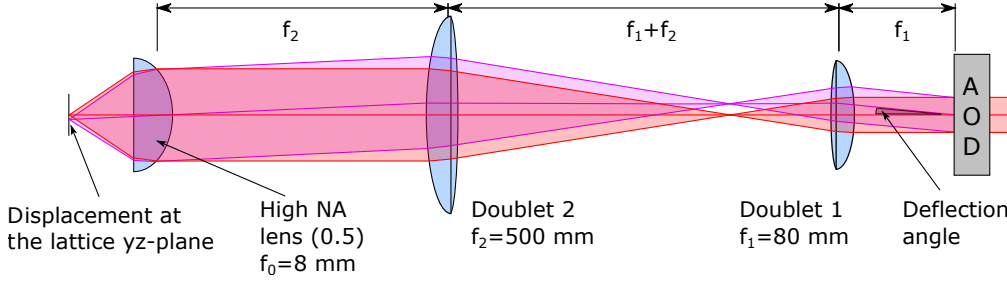


Figure 3.3: **Simplified diagram and ray tracing of the optical transfer system (not to scale).** It is designed to convert the full range angular deflection of the AOD $\theta_{\text{AOD}} = 2.6^\circ$ to a displacement of the focus at the lattice plane of $a_0 = 60 \mu\text{m}$ and to focus to waist of $\approx 0.7 \mu\text{m}$.

the relative positions of the lenses are strictly related to their focal lengths (see Fig. 3.3). Using purely ray optics, considering only perfect lenses, and with the small angle approximation, the displacement is given by

$$a_0 = \frac{f_1}{f_2} f_0 \theta_{\text{AOD}} . \quad (3.5)$$

From the design, with $f_0 = 8 \text{ mm}$ for the high-NA lens and the values of the doublet lenses already given, an effective scan angle of the AOD $\theta_{\text{AOD}} = 2.6^\circ$ (average of the measured ones of the two axes in Sec. 3.1.2) corresponds to a displacement $a_0 = 60 \mu\text{m}$. This distance gives us the freedom to address atoms inside the cavity region ($w_0 \approx 13 \mu\text{m}$) as well as outside, thus offering the possibility to generate the desired patterns that can be shifted later.

The second function of the system is to obtain the smallest waist of the push-out beam at the lattice plane, now considering Gaussian optics. For this, the telescope serves as a beam expander to cover the full effective aperture of the high-NA lens and thus use its full focusing power. As a result, the input beam of the AOD (collimated, $w_0 \approx 1 \text{ mm}$) is focused at the lattice position to a waist of $w'_0 \approx 0.7 \mu\text{m}$. Compared to the lattice constant of 430 nm , we see that no single-site addressing is possible, since the spot size covers more than three lattice sites. However, we estimate that we can achieve single atom addressing by choosing the appropriate targets given the low filling factor of our trap.

3.2 Characterization and optimization of the addressing system

Once the addressing setup is implemented in the main experimental setup, we proceed to determine experimentally the characteristics of the addressing beam and to optimize the push-out effect. Although our setup at this point already allows 2D addressing, for the

rest of this project we used only 1D addressing along the optical conveyor belt (y -axis). However, given the radial symmetry of the system, we assume that the performance along the z -axis is qualitatively equivalent and the quantitative characterization very similar.

We were mainly interested in two different aspects. On the one hand we wanted to characterize the efficiency and the selectivity of the push-out effect depending on the power of the beam. These are the main properties that describe the performance of an addressing system. The *efficiency* refers to the probability to succeed in the push-out of the target atoms, while the *selectivity* corresponds to the probability of not expelling neighboring atoms.

On the other hand we wanted to measure the displacement of the beam along the y -axis dipole trap as a function of the angular driving of the acousto-optic deflector. In this case we were interested in verifying the linear behavior and the transformation factor predicted from the design of the optical transfer system.

3.2.1 Dependence of the push-out effect on the beam power

The range of the push-out is determined by the beam waist at the position of the lattice and by the intensity. But for the selectivity we have to take into account that it is more efficient to push-out atoms from the trap than to heat them out (see Section 3.1.1). Hence, it should be possible to choose a value for the beam power to achieve efficient push-out close to the beam center and low heat-out probability in the adjacent lattice sites.

The dependence of both properties on the power of the beam is highly non-linear, implying a trade-off that has to be investigated to find an optimum push-out value. It turns out that we can obtain good figures of merit for these properties, from the mean spatial distribution of the fluorescence detected after a push-out event.

The basic experimental sequence for this measurement is the following: first we load a few atoms from the MOT into the conveyor belt (see Ch. 1) and move them to the position of the cavity. During this measurement, exclusively the optical lattice of the conveyor belt is activated, since for the moment we only consider 1D addressing. Subsequently, the dipole trap depth is lowered adiabatically to ≈ 0.5 mK to increase the push-out efficiency, and the push-out beam is turned on during 100 ms, after which the EMCCD camera captures an image with an exposure of 10 ms.

If we average over more than 500 shots, we obtain the 2D map of the mean fluorescence on the yz -plane that we show in Fig. 3.4a, where the *hole* generated by the push-out beam can be clearly seen. Since in this case the optical lattice is one dimensional along the y -axis, for this level of analysis we can consider that the distribution along the z -axis contains no useful information. Then, integrating the counts along the z direction yields a trace of the total fluorescence as a function of the position in the conveyor belt lattice

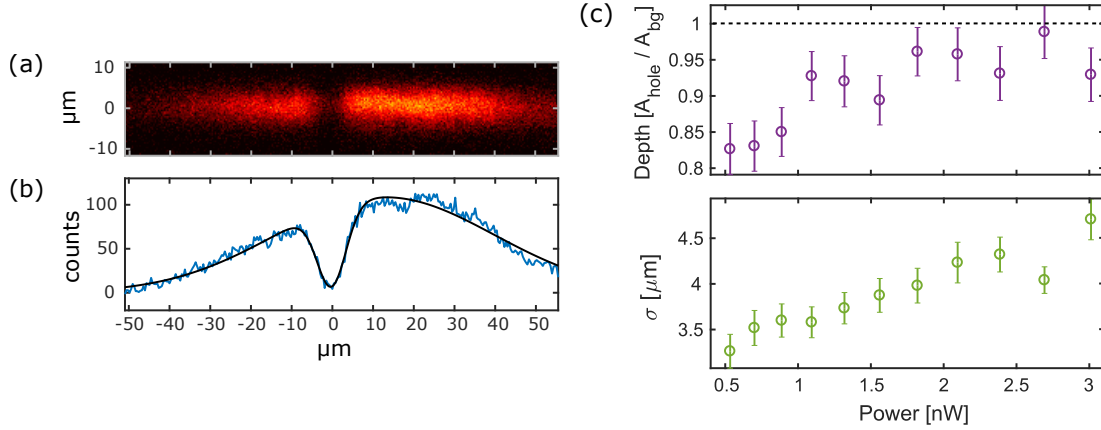


Figure 3.4: **Characterization of the effect of the on the push-out process.** (a) Average image of > 500 fluorescence images of atoms in the yz -plane of the lattice taken after a push-out event with $P \approx 1$ nW, where the *hole* created by the beam is clearly visible. (b) Trace of the fluorescence versus position in the lattice, obtained by integrating the counts in the z direction (blue line). We extract the *depth* and the *width* of the fluorescence dip with a double Gaussian fit (black line). (c) Plot of the relative depth A_{hole}/A_{bg} and width σ_{hole} of the fluorescence dip versus the power of the push-out beam. The error bars represent the were calculated with the standard bootstrapping resampling technique.

(Fig. 3.4b).

To gain more information from the trace, we fit it with the expression $f(y) = G_{bg}(y) - G_{hole}(y)$ where both functions $G(y)$ are standard Gaussian distributions along the y -axis, each one with respective free parameters: the peak amplitude A , the center position μ and the (half) width σ . Here $G_{bg}(y)$ accounts for the background distribution without the push-out event and is used for normalization, while $G_{hole}(y)$ gives us useful information about the geometry of the fluorescence dip. In fact, the normalized *depth* of the fluorescence dip A_{hole}/A_{bg} reflects the probability to push-out the target atoms, e.g. the efficiency. Furthermore, the *width* of the dip gives a measure of the radial range of the push-out effect, hence a figure of merit for the selectivity.

Now, to investigate how these parameters behave as a function of the push-out intensity, we repeat the same experimental sequence for different values of the push-out power. The results of A_{hole}/A_{bg} and σ_{hole} versus power are plotted in Figure 3.4c. As expected, we see that both parameters increment with the power: qualitatively we see that the depth follows a saturation curve with at least 95% suppression from $P \approx 1.7$ nW, while the width has a more linear behavior. For these measurements, the smallest width of the dip is $\sigma_{hole} \approx 3 \mu\text{m}$.

3.2.2 Calibration of the push-out beam displacement

It is fundamental for a precise addressing to know the exact correspondence between the control parameter, e.g. the RF driving frequency of the deflector (or deflection angle), and the position of the beam at the lattice, after the implementation in the main experiment. Therefore, we now want to determine experimentally the displacement of the focus of the push-out beam along the y -axis of the optical trap, when changing the AOD frequency, and thus the deflection angle. From the design of the optical transfer system (Eq. 3.5) we expect a linear dependence of the beam displacement on the angular deflection of the AOD, which is in turn a linear function of the RF driving frequency of the deflector (Sec. 3.1.2).

For this measurement we followed the same basic experimental sequence as described in the previous part to obtain pictures of the atoms after a push-out event (Sec. 3.2.1). Again, we average over more than 500 shots and integrate the counts along the z -axis. We also fit the dip in the resulting trace with a Gaussian, but in this case we are only interested in the parameter μ_{hole} which corresponds to the position of the beam center. Then, the same procedure is repeated for a fixed power $P \approx 1$ nW while changing the RF frequency of the AOD, as shown in Fig. 3.5b where we can observe the displacement of the hole created in the atomic distribution.

The measured position of the beam for 11 different frequencies between 91 and 123 MHz is plotted as a function of the AOD frequency in Figure 3.5b. We observe that the behavior of the displacement is perfectly linear as expected. From the plot we obtain the value of the slope of $\approx -1.48 \mu\text{m}/\text{MHz}$, and considering the calibration of the deflector from Section 3.1.2 ($m_y \approx 0.06^\circ/\text{MHz}$), it corresponds to a transformation factor of $25 \mu\text{m}/^\circ$.

3.3 Conclusions and next steps

In this chapter we analyzed the capabilities of our newly implemented addressing setup, with the investigation of its efficiency and selectivity, and the longitudinal reach along the optical lattice.

It can be noted that the smallest width that we measured was $\sigma_{\text{hole}} \approx 3 \mu\text{m}$, which is bigger than our rough expectations: the designed beam waist is $w_0 \approx 0.7 \mu\text{m}$, although these quantities are not directly comparable. Nevertheless, still more measurements have to be made at lower power, where we expect the width of the dip to become constant in some range. This value would give an estimation of the minimum range of the push-out effect, and thus of the ultimate selectivity of the addressing system. In addition, for a proper minimization of the width, the position of the lenses of the optical transfer system should be further optimized to reach the design parameters.

The results make clear the trade-off between push-out efficiency and selectivity, or

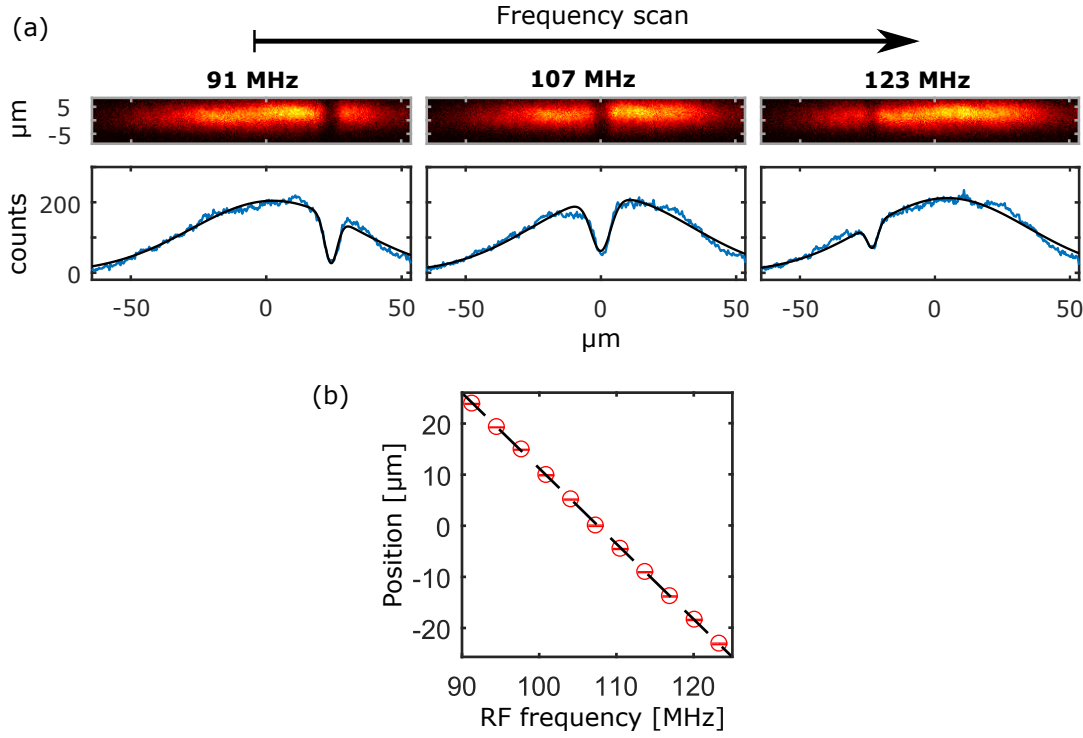


Figure 3.5: **Calibration of the push-out beam displacement.** (a) Sequence showing the movement of the beam along the horizontal dipole trap when scanning the RF driving frequency of the AOD y -axis. The beam position is obtained by fitting the dip in the trace of integrated counts, with the same technique as in Fig. 3.4. (b) Plot of the position of the push-out beam versus $f_{\text{RF},y}$ of the AOD. The error bars represent the standard deviation calculated with the bootstrapping resampling technique. The calibration slope obtained from the linear fit is $\approx -1.48 \mu\text{m}/\text{MHz}$.

in other words maximizing the depth and minimizing the width of the fluorescence dip. Accordingly, to find an optimum value of the push-out power we would need to define a cost function of both parameters, that would depend on the aim and specific factors of each experimental sequence. For example, if the filling factor of the lattice is set to very low, then the σ_{hole} parameter is less critical since there will be very few neighboring atoms in the push-out range. Yet, this goes beyond the extent of this work.

Now regarding the transverse displacement of the addressing beam, the measured transformation factor was $25 \mu\text{m}/^\circ$, not far from the value of $23 \mu\text{m}/^\circ$ expected from the design. We attribute this small discrepancy to the lack of final optimization of the optical setup of the addressing system.

The measurements shown here are the first step towards the optimization of the push-out process, and a good starting point for the fine tuning of the parameters.

An application of the setup that could be achieved in the near future, is the automatic

selection of predefined atomic patterns from a probabilistic loading. For this, an algorithm was already programmed to process the position of the atoms in the lattice, determine the target atoms for highest probability to create the pattern, and send the feedback signal to the AOD for a shoot-out sequence.

Summary and outlook

In this thesis, I have presented two key additions to the main experimental setup in our lab. These constitute the basic tools for controlling the number of atoms and their position inside the fiber-cavity.

First I described the newly implemented fluorescence imaging scheme, based on the D1 line of ^{87}Rb atoms, that is independent of the cavity effects, thus avoiding the enhanced collection efficiency of the cavity and circumventing the problem of decreased fluorescence observed when imaging in the D2 line. This ensures a consistent and robust method for 2D position determination of the trapped atoms inside the cavity. Still, a cooling method needs to be implemented to make the imaging process non-destructive.

Furthermore, we showed the implementation of a setup designed for two-dimensional addressing of atoms in the optical lattice with a push-out optical beam. This system will enable the selection of atom patterns, with predefined number and position, that interact with the cavity mode. The proof of principle was demonstrated with 1D addressing and will be extended to 2D, after further optimization to achieve single-atom selectivity.

In the first place, these upgrades will improve the degree of control over our atom-cavity system, given the possibility to select a deterministic number of atoms coupled to the cavity mode, permitting a pre-selection option apart of the post-selection method used until now. This will boost the efficiency of the data collection by improving the statistics and increasing the reproducibility of the results. Ultimately, the work presented here represents the first step towards the future realization of dissipative bipartite entanglement, as it provides essential tools for the implementation of the protocol.

An application of the system that could be achieved in the near future, is the automatic selection of predefined atomic patterns from a probabilistic loading, in real-time. For this, an algorithm was already programmed to process the position of the atoms in the lattice [27, 54], to determine the target atoms for highest probability to create the pattern, and send the feedback signal to the AOD for a shoot-out sequence.

Another application of the single-atom addressing scheme is the selective control of the quantum state of individual atoms by coherent Raman manipulation. This can be readily implemented by using an already existing Raman beam as the light source [61], instead of the push-out beam. In addition, both imaging and addressing setups could be extended to provide 3D capabilities [51]. This would be realized by replicating the systems, now using one of the high-NA lenses in the perpendicular direction. Such addressing of single-qubit in a three-dimensional optical lattice would pave the way to a scalable system for quantum computation.

Bibliography

- [1] A. Einstein, *Zur Quantentheorie der Strahlung*, *Physikalische Zeitschrift* **18** (1917).
- [2] D. T. Haar, *The Old Quantum Theory*. Pergamon, Oxford, 1967.
- [3] R. Loudon, *The Quantum Theory of Light*. Clarendon Press, Oxford, 1973.
- [4] P. A. M. Dirac, *The Quantum Theory of the Emission and Absorption of Radiation*, *Proceedings of the Royal Society of London A: Mathematical, Physical and Engineering Sciences* **114** no. 767, (1927) 243–265.
- [5] E. M. Purcell, *Spontaneous emission probabilities at radio frequencies*, in *Physical Review*, pp. , 681+. 1946.
- [6] S. Haroche and J. M. Raimond, *Exploring the Quantum: Atoms, Cavities, and Photons*. Oxford Graduate Texts. OUP Oxford, 2006.
- [7] E. Jaynes and F. Cummings, *Comparison of quantum and semiclassical radiation theories with application to the beam maser*, *Proceedings of the IEEE* **51** no. 1, (1963) 89–109.
- [8] S. Haroche and D. Kleppner, *Cavity Quantum Electrodynamics*, *Physics Today* **42** no. 1, (1989) 24–30, <http://dx.doi.org/10.1063/1.881201>.
- [9] M. J. Kastoryano, F. Reiter, and A. S. Sørensen, *Dissipative Preparation of Entanglement in Optical Cavities*, *Physical Review Letters* **106** no. 9, (2011) 090502.
- [10] F. Reiter, M. J. Kastoryano, and A. S. Sørensen, *Driving two atoms in an optical cavity into an entangled steady state using engineered decay*, *New Journal of Physics* **14** no. 5, (2012) 053022.
- [11] T. Pellizzari, S. A. Gardiner, J. I. Cirac, and P. Zoller, *Decoherence, Continuous Observation, and Quantum Computing: A Cavity QED Model*, *Physical Review Letters* **75** no. 21, (1995) 3788–3791.
- [12] F. De Martini and M. C. (Eds.), *Experimental Quantum Computation and Information, in Proceedings of the International School of Physics Enrico Fermi*. IOS Press, Amsterdam, 2002.

- [13] R. Miller, T. E. Northup, K. M. Birnbaum, A. Boca, A. D. Boozer, and H. J. Kimble, *Trapped atoms in cavity QED: coupling quantized light and matter*, *Journal of Physics B: Atomic, Molecular and Optical Physics* **38** no. 9, (2005) S551–S565.
- [14] L. M. Duan, M. D. Lukin, J. I. Cirac, and P. Zoller, *Long-distance quantum communication with atomic ensembles and linear optics*, *Nature* **414** no. 6862, (2001) 413–418, [arXiv:0105105 \[quant-ph\]](#).
- [15] H. P. Specht, C. Nölleke, A. Reiserer, M. Uphoff, E. Figueroa, S. Ritter, and G. Rempe, *A single-atom quantum memory*, *Nature* **473** (2011) 190–193.
- [16] J. M. Raimond, M. Brune, and S. Haroche, *Manipulating quantum entanglement with atoms and photons in a cavity*, *Rev. Mod. Phys.* **73** no. 3, (2001) 565–582.
- [17] X.-Y. Chen, L.-T. Shen, Z.-B. Yang, H.-Z. Wu, and M.-F. Chen, *Engineering W-type steady states for three atoms via dissipation in an optical cavity*, *Journal of the Optical Society of America B* **29** no. 6, (2012) 1535.
- [18] R. Sweke, I. Sinayskiy, and F. Petruccione, *Dissipative preparation of large W states in optical cavities*, *Physical Review A* **87** no. 4, (2013) 042323.
- [19] F. Reiter, D. Reeb, and A. S. Sørensen, *Scalable Dissipative Preparation of Many-Body Entanglement*, *Physical Review Letters* **117** no. 4, (2016) 040501.
- [20] J. Gallego, *Fiber-based cavities for strong coupling with atomic ensembles*. PhD thesis, Rheinische Friedrich-Wilhelms-Universität Bonn, (in preparation).
- [21] D. Hunger, T. Steinmetz, Y. Colombe, C. Deutsch, T. W. Hänsch, and J. Reichel, *A fiber Fabry–Perot cavity with high finesse*, *New Journal of Physics* **12** no. 6, (2010) 65038.
- [22] J. Gallego, S. Ghosh, S. K. Alavi, W. Alt, M. Martinez-Dorantes, D. Meschede, and L. Ratschbacher, *High-finesse fiber Fabry–Perot cavities: stabilization and mode matching analysis*, *Applied Physics B* **122** no. 3, (2016) 47.
- [23] D. Schrader, S. Kuhr, W. Alt, M. Müller, V. Gomer, and D. Meschede, *An optical conveyor belt for single neutral atoms*, *Applied Physics B* **73** no. 8, (2001) 819–824.
- [24] W. S. Bakr, J. I. Gillen, A. Peng, S. Fölling, and M. Greiner, *A quantum gas microscope for detecting single atoms in a Hubbard-regime optical lattice*, *Nature* **462** no. 7269, (2009) 74–77.
- [25] J. F. Sherson, C. Weitenberg, M. Endres, M. Cheneau, I. Bloch, and S. Kuhr, *Single-atom-resolved fluorescence imaging of an atomic Mott insulator*, *Nature* **467** no. 7311, (2010) 68–72.
- [26] W. Alt, *Optical control of single neutral atoms*. PhD thesis, Rheinische Friedrich-Wilhelms-Universität Bonn, 2004.

-
- [27] M. Karski, *State-selective transport of single neutral atoms*. PhD thesis, Rheinische Friedrich-Wilhelms-Universität Bonn, 2010.
- [28] M. Martínez-Dorantes, *Fast non-destructive internal state detection of neutral atoms in optical potentials*. PhD thesis, Rheinische Friedrich-Wilhelms-Universität Bonn, 2016.
- [29] P. Maunz, T. Puppe, I. Schuster, N. Syassen, P. W. H. Pinkse, and G. Rempe, *Cavity cooling of a single atom*, *Nature* **428** (2004) 50–52.
- [30] D. A. Steck, *Rubidium 87 D Line Data*, (revision 2.1.5, 13 january 2015), 2001. <http://steck.us/alkalidata>.
- [31] M. Fleischhauer, A. Imamoglu, and J. P. Marangos, *Electromagnetically induced transparency: Optics in coherent media*, *Reviews of Modern Physics* **77** no. 2, (2005) 633–673.
- [32] H. J. Metcalf and P. van der Straten, *Laser Cooling and Trapping*. Graduate Texts in Contemporary Physics. Springer New York, New York, NY, 1999.
- [33] D. A. Steck, *Quantum and Atom Optics*, (revision 0.12.0, 16 may 2017), 2007. <http://steck.us/teaching>.
- [34] C.-Y. Shih and M. S. Chapman, *Nondestructive light-shift measurements of single atoms in optical dipole traps*, *PHYSICAL REVIEW A* **87** no. 063408, (2013).
- [35] K. B. MacAdam, A. Steinbach, and C. Wieman, *A narrow-band tunable diode laser system with grating feedback, and a saturated absorption spectrometer for Cs and Rb*, *American Journal of Physics* **60** no. 12, (1992) 1098–1111.
- [36] L. Ricci, M. Weidemüller, T. Esslinger, A. Hemmerich, C. Zimmermann, V. Vuletic, W. König, and T. W. Hänsch, *A compact grating-stabilized diode laser system for atomic physics*, *Optics Communications* **117** no. 5-6, (1995) 541–549.
- [37] C. E. Wieman and L. Hollberg, *Using diode lasers for atomic physics*, *Review of Scientific Instruments* **62** no. 1, (1991) 1–20.
- [38] W. Demtröder, *Laser spectroscopy. Vol. 2, Experimental techniques*. Springer-Verlag, 2008.
- [39] C. Wieman and T. W. Hänsch, *Doppler-Free Laser Polarization Spectroscopy*, *Physical Review Letters* **36** no. 20, (1976) 1170–1173.
- [40] M. L. Harris, C. S. Adams, S. L. Cornish, I. C. McLeod, E. Tarleton, and I. G. Hughes, *Polarization spectroscopy in rubidium and cesium*, *Physical Review A* **73** no. 6, (2006) 062509, [arXiv:0509157 \[physics\]](https://arxiv.org/abs/0509157).

- [41] D. Groswasser, A. Waxman, M. Givon, G. Aviv, Y. Japha, M. Keil, and R. Folman, *Retroreflecting polarization spectroscopy enabling miniaturization*, *Review of Scientific Instruments* **80** no. 9, (2009) 93103.
- [42] D. A. Smith and I. G. Hughes, *The role of hyperfine pumping in multilevel systems exhibiting saturated absorption*, *American Journal of Physics* **72** no. 5, (2004) 631–637.
- [43] P. Siddons, C. S. Adams, C. Ge, and I. G. Hughes, *Absolute absorption on the rubidium D lines: comparison between theory and experiment*, *Journal of Physics B: Atomic, Molecular and Optical Physics* **41** no. 15, (2008) 155004, [arXiv:0805.1139v1](#).
- [44] A. Alberti, C. Robens, W. Alt, S. Brakhane, M. Karski, R. Reimann, A. Widera, and D. Meschede, *Super-resolution microscopy of single atoms in optical lattices*, *New Journal of Physics* **18** no. 5, (2016) 53010.
- [45] M. Khudaverdyan, *A controlled one and two atom-cavity system*. PhD thesis, Rheinische Friedrich-Wilhelms-Universität Bonn, 2009.
- [46] R. Reimann, *Cooling and Cooperative Coupling of Single Atoms in an Optical Cavity*. PhD thesis, Rheinische Friedrich-Wilhelms-Universität Bonn, 2014.
- [47] R. Scheunemann, F. S. Cataliotti, T. W. Hänsch, and M. Weitz, *Resolving and addressing atoms in individual sites of a CO₂-laser optical lattice*, *Phys. Rev. A* **62** no. 5, (2000) 51801.
- [48] M. Karski, L. Förster, J.-M. Choi, A. Steffen, N. Belmechri, W. Alt, D. Meschede, and A. Widera, *Imprinting patterns of neutral atoms in an optical lattice using magnetic resonance techniques*, *New Journal of Physics* **12** no. 6, (2010) 65027.
- [49] P. Würtz, T. Langen, T. Gericke, A. Koglbauer, and H. Ott, *Experimental Demonstration of Single-Site Addressability in a Two-Dimensional Optical Lattice*, *Phys. Rev. Lett.* **103** no. 8, (2009) 80404.
- [50] C. Weitenberg, M. Endres, J. Sherson, M. Cheneau, P. Schausz, T. Fukuhara, I. Block, and S. Kuhr, *Single-spin addressing in an atomic Mott insulator*, *Nature* **471** (2011) 319–324.
- [51] Y. Wang, X. Zhang, T. A. Corcovilos, A. Kumar, and D. S. Weiss, *Coherent Addressing of Individual Neutral Atoms in a 3D Optical Lattice*, *Phys. Rev. Lett.* **115** no. 4, (2015) 43003.
- [52] A. Neuzner, M. Körber, O. Morin, S. Ritter, and G. Rempe, *Interference and dynamics of light from a distance-controlled atom pair in an optical cavity*, *Nature Photonics* **10** no. 5, (2016) 303–306.

-
- [53] M. Endres, H. Bernien, A. Keesling, H. Levine, E. R. Anschuetz, A. Krajenbrink, C. Senko, V. Vuletic, M. Greiner, and M. D. Lukin, *Atom-by-atom assembly of defect-free one-dimensional cold atom arrays*, *Science* **354** no. 6315, (2016) 1024–1027.
- [54] R. Jindra, *Positioning of Single Atoms in a Dipole Trap*, Master’s thesis, Technische Universität Wien, 2015.
- [55] S. Kuhr, *A controlled quantum system of individual neutral atoms*. Phd thesis, Rheinische Friedrich-Wilhelms-Universität Bonn, 2003.
- [56] M. Bass and Optical Society of America., *Handbook of optics*. McGraw-Hill, 1995.
- [57] N. Uchida, *Optical Properties of Single-Crystal Paratellurite (TeO_2)*, *Physical Review B* **4** no. 10, (1971) 3736–3745.
- [58] T. Yano, M. Kawabuchi, A. Fukumoto, and A. Watanabe, *TeO_2 anisotropic Bragg light deflector without midband degeneracy*, *Citation: Appl. Phys. Lett* **26** no. 689, (1975).
- [59] R. Dixon, *Acoustic diffraction of light in anisotropic media*, *IEEE Journal of Quantum Electronics* **3** no. 2, (1967) 85–93.
- [60] ISOMET, *Acousto-Optic Modulation, Application Note AN0510*, <http://www.isomet.com/appnotes.html>.
- [61] L. Paulet, *Raman and Microwave Manipulation of Small Atomic Ensembles*, Master’s thesis, Rheinische Friedrich-Wilhelms-Universität Bonn, 2014.

Appendix

Effective scattering rate in a three-level system with two light fields

In our case the system is more complicated than a two-level one, since there is no closed hyperfine transitions in the D1 line of ^{87}Rb (Fig. 2.2a), and hence we address two similarly strong transitions with two lasers. Nevertheless, the photons that we detect come from combined fluorescence of both scattering processes. For the given illumination scheme we expect the atoms to scatter photons at an effective rate related to the individual scattering rates of the driven transitions.

For a qualitative description of the scattering behavior, we consider an atom with two ground states $|g_1\rangle$ and $|g_2\rangle$, with instantaneous respective populations ρ_1 and ρ_2 , and a single common excited state $|e\rangle$ that decays instantaneously with equal probability to either of the ground levels. It interacts with two electric fields, with the same amplitude, that drive the transitions $|g_1\rangle \rightarrow |e\rangle$ and $|g_2\rangle \rightarrow |e\rangle$ with scattering rates R_{1e} and R_{2e} respectively.

The rate equations describing the dynamics of this system are then

$$\begin{aligned}\dot{\rho}_1 &= \frac{1}{2}(-R_{1e}\rho_1 + R_{2e}\rho_1) \\ \dot{\rho}_2 &= \frac{1}{2}(-R_{2e}\rho_2 + R_{1e}\rho_1) .\end{aligned}$$

and we can find their steady-state solutions that fulfill the conditions

$$R_{1e}\rho_{1,ss} = R_{2e}\rho_{2,ss} \quad \text{and} \quad \rho_{1,ss} + \rho_{2,ss} = 1 .$$

Now, in steady state, the atom will scatter photons at an effective rate given by

$$\tilde{R}_{sc} = R_{1e}\rho_{1,ss} + R_{2e}\rho_{2,ss}$$

and after some algebra we find the result

$$\tilde{R}_{sc} = 2 \frac{R_{1e} R_{2e}}{R_{1e} + R_{2e}} \quad (\text{A.1})$$

or written in another way

$$\frac{1}{\tilde{R}_{sc}} = \frac{1}{2} \left(\frac{1}{R_{1e}} + \frac{1}{R_{2e}} \right) . \quad (\text{A.2})$$

We can now consider two cases: if $R_{1e} = R_{2e} = R$, the effective rate will also have the same value $\tilde{R}_{sc} = R$. However, if one of the rates dominates, e.g. $R_{1e} \gg R_{2e}$, we find that $\tilde{R}_{sc} \approx 2R_{2e}$, so the effective scattering rate will be limited by the slower transition. This is the case because the faster transition will just optically pump all the population to the other ground level, e.g. fill $|g_2\rangle$ and empty $|g_1\rangle$.

Acknowledgements

In the first place, I would like to thank specially Professor Dieter Meschede for giving me the opportunity to become a part of his group and work on this research project which was deeply interesting and rich with insightful learning.

I am also thankful to Professor Stefan Linden for accepting my invitation as co-supervisor of my thesis.

I wish to acknowledge the Bonn-Cologne Graduate School of Physics and Astronomy (BCGS), and the University of Guadalajara (UdeG), for the financial support that gave me the possibility to take part in this high-level master program.

I also would like to extend my special gratitude to Dr. Miguel Martínez Dorantes and Dr. Deepak Pandey, my direct research project supervisors, for their patient and masterful guidance, and their great involvement when things where not working as expected. I also want to thank Dr. Wolfgang Alt for the useful critiques and constructive suggestions he provided.

Furthermore, I am particularly grateful with all current members of the FCQED group, to which I had the luck to belong during this project. In particular I thank my colleagues José Gallego and Tobias Macha, for their patience, the knowledge they shared, and their valuable technical support during the development of this work.

Estoy profundamente agradecido con Natalia, quién me ha acompañado durante este proceso, y cuyo amor y apoyo fueron esenciales para la culminación de esta estapa.

Finalmente, quiero agradecer a mi familia, en especial a mis padres, por el apoyo incondicional que me han dado y la motivación que transmiten para seguir adelante, aprendiendo y creciendo como persona.